5-2015

Experimental and analytical study of an open cathode polymer electrolyte membrane fuel cell.

Alex Martin Bates
University of Louisville

EXPERIMENTAL AND ANALYTICAL STUDY OF AN OPEN CATHODE POLYMER ELECTROLYTE MEMBRANE FUEL CELL

By

Alex Martin Bates
B.S., University of Louisville, 2014

A Thesis
Submitted to the Faculty of the
University of Louisville
J. B. Speed School of Engineering
as Partial Fulfillment of the Requirements
for the Professional Degree

MASTER OF ENGINEERING

Department of Mechanical Engineering

May 2015

EXPERIMENTAL AND ANALYTICAL STUDY OF AN OPEN CATHODE POLYMER ELECTROLYTE MEMBRANE FUEL CELL

Submitted by: Alex Martin Bates

A Thesis Approved On

(Date)

by the Following Reading and Examination Committee:

Sam D. Park, Thesis Director

Ellen G. Brehob

Kyung A. Kang

ACKNOWLEDGMENTS

This work was supported by the DGIST R&D Program of the Ministry of Education, Science and Technology of Korea (13-BD-01).

ABSTRACT

In this thesis four different fuel cell designs were simulated with consideration for electrochemical effects, reactant species transport, and heat transfer. Simulation results include the mass fraction of hydrogen, oxygen, and water, temperature gradient, pressure gradient, and velocity profile. One of the fuel cell designs was experimentally tested using two different membrane electrolyte assemblies; one high performance and the other high durability. The polarization curve resulting from simulation compares well with the polarization curve produced by experimental work.

A 16 cell fuel cell stack was simulated with consideration for stack compression. The same fuel cell stack was tested experimentally for compression using pressure sensitive films. Compression testing was performed in order to find areas of low compression and high compression. Low compression regions lead to high contact resistance which degrades the performance of the fuel cell. High compression regions can cause damage to the thin and brittle membrane electrolyte assemblies. A good correlation was found between the compression pattern resulting from simulation and experimental work.

TABLE OF CONTENTS

NOMENCLATURE

A_c	=	Cathodic Tafel slope (V)
cH_2_ref	=	Hydrogen reference concentration (mol m^{-3})
$chcs.c\_wH_2$	=	Hydrogen molar concentration (mol m^{-3})
$chcs2.c\_wO_2$	=	Oxygen molar concentration (mol m^{-3})
cO_2_ref	=	Oxygen reference concentration (mol m^{-3})
C_p	=	Heat capacity at constant pressure (J kg^{-1} K^{-1})
F	=	Faraday's constant; 96487 (C mol^{-1})
$\boldsymbol{i}_l$	=	Electrolyte current density (A m^{-2})
i_{loc}	=	Local charge transfer current density (A m^{-2})
i_0	=	Exchange current density (A m^{-2})
$\boldsymbol{i}_s$	=	Electrode current density (A m^{-2})
$\boldsymbol{j}_i$	=	Mass flux (kg s^{-1} m^{-2})
k	=	Thermal conductivity (W m^{-1} K^{-1})
K_{br}	=	Permeability (m^2)
$\boldsymbol{l}$	=	Entrance length (m)
$\boldsymbol{n}$	=	Surface normal
n_m	=	Number of participating electrons
p	=	Pressure (Pa)
Q	=	Heat source/sink (W m^{-3})
Q_b	=	Boundary heat source (W m^{-2})
Q_{br}	=	Source term (kg m^{-3} s^{-1})
R	=	Universal gas constant; 8.314 (J mol^{-1} K^{-1})
T	=	Temperature (K)
$\boldsymbol{u}$	=	Velocity field (m s^{-1})
$v_{i,m}$	=	Stoichiometric coefficient
α_a	=	Anodic transfer coefficient
α_c	=	Cathodic transfer coefficient

β_F = Forchheimer drag (kg m^{-4})

ϵ_p = Porosity

η = Overpotential (V)

μ = Dynamic viscosity (Pa s)

ρ = Density (kg m^{-3})

σ_l = Electrolyte conductivity (S m^{-1})

σ_s = Electrode conductivity (S m^{-1})

ϕ_l = Electrolyte potential (V)

ϕ_s = Electric potential (V)

ω_i = Mass fraction

LIST OF TABLES

LIST OF FIGURES

I. INTRODUCTION

Energy resources are a constant topic of debate in today's society. Researchers are continuously working toward sustainable, clean, and high efficiency energy. As society moves away from the burning of fossil fuels, many new systems such as solar, wind, and hydrogen power are increasingly becoming available on the market. Currently, none of the new systems appears to be able to completely fulfil energy demands. As such, tomorrow's society will likely require many different energy systems, each one being more suitable for a specific set of energy requirements. Fuel cells are able to harness the power of hydrogen gas to directly produce electricity with only heat and water as a byproduct.

A. Fuel Cell Fundamentals

Fuel cells convert the chemical energy of a hydrogen and oxygen reaction directly into electrical energy without an intermediate mechanical process. At a basic level, a fuel cell consists of a porous anode and cathode, separated by an electrolyte layer. In fuel cells the electrolyte layer is called a proton exchange membrane or polymer electrolyte membrane (PEM). Hydrogen diffuses into the anode while oxygen diffuses into the cathode. The PEM contains a catalyst, typically platinum, on both sides and is made from a material that only allows the passage of hydrogen ions and blocks the passage of electrons. When hydrogen reaches the catalyst on the PEM, the following reaction occurs

$$2H_2 \rightarrow 4H^+ + 4e^- \quad (1)$$

Hydrogen ions pass through the PEM into the cathode while electrons flow out of the cell through an electrical circuit. When oxygen in the cathode reaches the catalyst on the PEM, the following reaction occurs

$$O_2 + 4e^- + 4H^+ \rightarrow 2H_2O \quad (2)$$

Oxygen reacts with hydrogen ions that passed through the PEM and electrons that flow into the cathode, completing an electrical circuit. The overall reaction in a hydrogen and oxygen fuel cell is

$$H_2 + \frac{1}{2}O_2 \rightarrow H_2O \quad (3)$$

Fuel cells require several other components to contain the reactant gases and allow for electrical power to be drawn. These components include, but are not limited to, flow plates, conduction plates, end plates, and gaskets. Flow plates route the flow of reactant gases across the porous anode and cathode, also known as the gas diffusion layers (GDLs). The combination of GDLs and PEM is termed the membrane electrode assembly (MEA). In some fuel cell arrangements a single flow plate will have channels for hydrogen flow on one side and oxygen on the other; these are referred to as bi-polar plates. Conduction plates are made from a material with a high electrical conductivity and are placed at both cathode and anode ends of a fuel cell. They are used to connect the fuel cell with an outside electrical circuit in order to draw a load. End plates are also placed at both cathode and anode ends of the fuel cell, outside of the conduction plates. End plates

allow for compression to be applied to the fuel cell so that sufficient electrical contact is made with the inner layers. End plates also provide a platform for the mounting of gas supply connectors and other apparatus such as a cooling and oxygen supply fan. Fuel cells come in all shapes, sizes, and complexities from 2.5 W micro fuel cells to a 15 MW fuel cell plant.

B. Fuel Cell Complications

At a fundamental level, fuel cells are very simple devices that convert chemical energy into electrical energy; however, difficulties arise in the assembly and structure of the fuel cell. Hydrogen gas is highly reactive and costly to produce; because of this it must be properly contained inside the fuel cell. Materials used to make the GDL and PEM are very thin and typically brittle. This combined with the compression required to maintain good electrical contact can result in hydrogen leakage due to cracks and pinholes in the MEA. Each cell in a fuel cell contains two GDLs, a PEM, and two gaskets between a set of flow plates. This results in a difficult balance of thickness, compressibility, structural integrity, gas leakage, and contact resistance.

Contact resistance is an important issue that results from difficulties in compressing a fuel cell stack. Compression is the result of bolts that connect both end plates and are tightened against the stack. The arrangement, number, size, and torque applied to the bolts will greatly affect the amount and distribution of compression within a fuel cell. In addition, different sizes and shapes of flow plates will result in different optimal bolt arrangements. In general, it is difficult to efficiently maintain compression in the center of each cell which can result in reduced performance of the fuel cell.

C. Research Purpose

Fuel cells are complex systems that require special materials, such as platinum, and advanced manufacturing techniques. This makes it expensive to build and test different fuel cell designs. Using computational fluid dynamics (CFD) software, it is possible to alleviate some of the time and expense involved in testing fuel cell designs. By building virtual models of desired designs and simulating them, a selection can be made before purchasing costly materials. In addition, simulations are a good platform from which to evaluate experimental data.

When optimizing a fuel cell, operating conditions must be balanced. For instance, increasing the air flow rate will always provide more oxygen and/or hydrogen for reaction; however, too much air flow can destroy the MEA and bring about challenges in keeping the fuel cell sealed. Optimization is of key importance to the advancement of fuel cells, as it increases performance and efficiency, making fuel cells more viable economically.

Examining fuel cell (FC) clamping pressure is important in determining contact resistance and its relation to FC efficiency. Research has shown that around 59% of the total power loss in a fuel cell can be due to contact resistance between the bi-polar plates and gas diffusion layers (GDLs) (Zhang 2006). Contact resistance is directly related to the applied clamping pressure and clamping configuration. Adjusting clamping pressure is an easy task to perform and should be optimized in order to take advantage of the benefits.

For optimization, clamping pressure must be balanced between competing effects. When clamping pressure is low, contact resistance between bi-polar plate and GDL will

be high. The material difference, machined carbon composite on porous carbon paper, requires pressure for good electrical contact. If the cells are not compressed enough, contact resistance will degrade performance. However, when too much clamping pressure is applied, other adverse effects will appear. The GDL can depress into the channels of the bi-polar plate, obstructing flow. This will lower efficiency and create hot spots that reduce the longevity of the FC. Also, the MEA is brittle and very susceptible to cracking or tearing under pressure. Any damage to those materials immediately reduces performance and can lead to further destruction of the FC. If clamping pressure is increased enough it will crack the brittle bi-polar plates as well.

D. Research Outline

The main objective of the research presented in this thesis was to study the hydrogen and oxygen, open-cathode, low temperature, PEM fuel cell. The open-cathode fuel cell design has straight through cathode channels to allow for air flow provided by a fan. The fan assisted air flow serves two purposes, providing oxygen to the cathode of the fuel cell for reaction and maintaining the fuel cell temperature. A low-temperature fuel cell operates at temperatures and humidity near ambient conditions. These features allow for the removal of certain components resulting in a lighter and more compact fuel cell system.

Several different methods were carried out to perform the stated objective. A single cell fuel cell was designed, built, and tested for performance, compression, structural integrity, and hydrogen gas leakage. A similar single cell fuel cell was modeled and simulated in 3D using finite element analysis (FEA). The program COMSOL was used to explore reactant species transport, current density from chemical reaction, and heat

transfer. The program SolidWorks was used to explore the effects of clamping pressure on a fuel cell containing several cells, otherwise known as a fuel cell stack.

The goal of the COMSOL simulation is to develop an experimentally validated 3D simulation of a single cell fuel cell considering effects of reactant species transport, chemical reaction, and heat transfer. The simulation can then be used to test the effects of changing flow field patterns and material properties with the goal of optimizing fuel cell designs without require the purchase and manufacture of expensive fuel cell components. Simulations for several different flow plate and flow pattern designs are presented in this these.

The goal of the SolidWorks simulation was to develop an experimentally validated 3D simulation of a fuel cell stack under compression. The simulation will give an insight into the stress distribution on the GDL which directly contributes to contact resistance through the fuel cell and regions of high stress that may result in damage to the fuel cell's brittle inner layers. The simulation developed will allow for future simulations to explore the compression effects of various bolt configurations and torques with a desire to provide sufficient and even compression throughout a fuel cell stack.

II. RELATED LITERATURE

A. Transport, Electrochemical, and Heat Transfer

To advance fuel cell technology, it is critical to effectively simulate fuel cell fluid transport and electrochemical reactions according to Wang et al. (Wang 2011). The main expense in a fuel cell currently is the platinum loading of the activation layer on the PEM. Without a major breakthrough in materials, increasing efficiency is required to push production of fuel cells. Simulation can be used as primary tool in increasing efficiencies of a fuel cell.

Sasmito et al. have tried to improve thermal management in a PEMFC using a new flow reversal technique (Sasmito 2012). They proposed a novel design where there is a rapid reversal of the cooling air responsible for convective cooling. They developed a mathematical model which includes the fuel cell stack, the ambient environment, and the fan as its important parameters (Sasmito 2012). The model also takes into consideration various mass flow phenomena including heat transfer conditions, conditions of mass and momentum transfer, conservation of charge, Ohm's law applications, and the modeling of the fan. Thermal equilibrium and the electro-osmotic drag of water are some important assumptions made. The commercial software GAMBIT was used by the authors. They simulated the condition of flow reversal by having a different boundary condition from 'fan' to 'interior'. The results showed that a more uniform current density is achieved during fuel cell operation with the flow reversal concept. The water content in the membrane is more uniform when using the flow reversal concept. Also, the authors were

able to show that increasing the rate of flow reversal results in a drop in uniformity of the current density (Sasmito 2012).

Various designs and considerations for better and improved thermal management were studied by Sasmito, Birgersson, and Mujumdar (Sasmito 2011). Some of the considerations and techniques involved the forced convection, edge air cooling with the help of fins, and forced and natural convection cooling. Mathematical modeling involved a 1D, 2-phase flow model with the assumptions of electro-osmotic drag, mass, energy, and charge equilibrium (Sasmito 2011). The Butler-Volmer equation was used to study overpotential, primarily at the cathode.

Ashgari et al. worked on developing a comprehensive thermal management system for a 5 kW PEMFC system (Ashgari 2011). They performed both experimental studies and modeling analysis. The experimental study consisted of a single cell and a five cell stack with the same anode and cathode flow fields. Optimum operating conditions were determined during the working of the cell (Ashgari 2011). The modeling analysis took into account the temperature distribution across the stack and the pressure drop across the flow field. Results indicated that there is a linear variation between the coolant flow rate and the pressure drop across the flow channels. Also, an increased coolant flow rate resulted in a uniform distribution of temperature and less parasitic losses (Ashgari 2011).

A CFD study on the effect of straight and serpentine flow fields was performed by Hashemi and coworkers (Hashemi 2012). The researchers developed a comprehensive 3D model for this purpose taking into consideration non-isothermal phenomena to mimic reality. Some of the more important assumptions include a steady flow condition, a laminar flow regime, ideal gas behavior and constant uniform activation overpotential.

The authors started with the continuity equation in 3D and then applied it to obtain mass and momentum balance. Charge conservation was also considered (Hashemi 2012). The results showed that the concentration gradient is steeper at the membrane interface than at the center. Also the serpentine flow field has a lower temperature gradient than the corresponding straight flow field. Another observation made is that the temperature distribution is more uniform in the serpentine flow field than the straight field. Also a higher current density is obtained near the flow field region due to greater ohmic potential drop (Hashemi 2012). Overall, the authors demonstrated that the serpentine flow fields showed a better temperature distribution and current density then the corresponding straight flow fields (Hashemi 2012).

Yazdi et al. developed a model of the cathode half-cell that includes the cathode side gas channels, GDL, and MEA (Yazdi 2010). Some assumptions made in this model include isothermal conditions and constant gas velocity. The oxygen flux is solved by Fick's first law, while reaction rate is represented by the Butler-Volmer equation. Limitations in the analytical solution required the assumption that the overvoltage potential is constant along the catalyst layer. This approach resulted in a very good estimation of a polarization curve (Yazdi 2010).

A dynamic model was developed by Ziogou et al. that considers temperature, humidity, pressure, and reactant mass flows (Ziogou 2011). The temperature is assumed to be uniform, and the pressure is homogeneous across the channels. This approach applied mass balance equations to solve for the reactant species concentration in each layer. Terms for diffusion, porosity, etc. were included where necessary. Energy balance was included to describe heat transfer and cooling effects. The Nernst equation was used

to obtain a voltage-current relationship. This model was experimentally validated and performed well as a dynamic fuel cell model. The model implemented some empirical formulas that must be recalculated for different designs.

A three-dimensional, multiphase, non-isothermal model with a domain of one flow channel was developed by Baghdadi et al. (Al-Baghdadi 2007). This model accounts for transport of gaseous species, liquid water, electrochemical effects, and water dissolved in the ion conducting polymer. Gas flow was described by the Navier-Stokes equations. Darcy's law controls flow in porous media. The Butler-Volmer equation was used to obtain current density. Heat generation was due to entropy change and irreversibility in activation overpotential (Al-Baghdadi 2007). This model enables the understanding of the many interacting phenomena, identifying limiting components and providing a computer aided tool for design and optimization. Additionally, the model shows that it is possible to calculate important parameters in the wetting behavior of the GDL and MEA.

Zhang studied the effects of operating parameters on the current density distribution in a PEM fuel cell to constrain the current density variation, correspondingly decreasing "pinholes" and improving the membrane reliability (Zhang 2007). The uniformity of local current density was constrained by the cell temperature, anode pressure, anode mass flow rate, and cathode mass flow rate (Zhang 2007). The orientation of the fuel cell was such that the anode is above the cathode in the vertical direction. The vertical orientation of the fuel cell leads to the largest cell performance, while the horizontal upward orientation is least effective for cell performance for a single air-breathing PEM fuel cell (Zhang 2007).

A study of PEM fuel cell thermal management with respect to micro-devices has been carried out by Ogedengbe (Ogedengbe 2009). He performed a detailed simulation of axial heat flow and conduction in micro-devices while varying pressure/velocity. Micro-channels were fabricated using silicon substrates. Maxwell's first order conditions were used to constrain the boundaries at the extremity of the micro-channel. Finite element analysis was used to develop a heat flow model. An important result obtained was that the interaction between molecules at the gas phase and the liquid phase is very important and can greatly affect the amount of heat generated (Ogedengbe 2009).

Shimpalee et al. developed governing equations to predict the temperature distribution inside a PEM fuel cell (Shimpalee 2000). The authors defined a control volume for analysis and solved the three dimensional Navier-Stokes equations to obtain a clear understanding of the effects of varying pressure and velocity. Important considerations taken into account during the solution of these equations were local variations in temperature and the electro-osmotic drag coefficient. The analysis was helpful in giving a picture of the temperature variation in a fuel cell. It also helps in providing the local current density at different regions in the PEMFC (Shimpalee 2000). Temperature distributions across the membrane surface and along the insulated boundary were all obtained from the simulation. Results show that the current density is affected by various factors including heat produced due to chemical reactions, phase change, etc. Fuel cell performance not only depends on the amount of the heat generated, but also on the variation of temperature during its operation (Shimpalee 2000).

Simulation of the thermal management of an air cooled system was performed by Tadbir et al. (Tadbir 2012). An air cooled system has many advantages over other

systems, namely, a lighter and less complex balance of plant. For an air cooled system to perform properly, the temperature distribution across the PEM fuel cell has to be correctly modeled and controlled. The authors also performed a modeling study on the electrical and thermal conductivity of the bipolar plates (Tadbir 2012). The main model consisted of three dimensional differential equations to solve for heat flow through the system. The net thermal conductivity of the system can be modeled based on thermal resistances in each direction. The model was experimentally validated using a Ballard fuel cell system (Tadbir 2012).

Zong et al. studied and modeled a PEM fuel cell with non-uniform stack temperature to effectively manage the heat balance of the system (Zong 2006). They developed a non-isothermal and non-isobaric thermal model of the system for this purpose. Modeling was done based on temperature variations locally at different points within the PEM fuel cell; from this and using the requisite boundary conditions, solutions were obtained (Zong 2006). The study concluded that parameters such as current density, output voltage, stack temperatures, steam pressures, etc. can be predicted based on accurately solving the differential equations (Zong 2006).

Thermal analysis of PEMFCs is especially important for air cooled cells and was investigated by Shahsavari et al. (Shahsavari 2012). The authors developed a 3D mathematical model for this purpose. They proceeded by choosing the governing equations such as conservation of energy, mass, and momentum. Water vapor was produced while running the fuel cell and was accounted for by considering it as a flux boundary condition in molar quantities (Shahsavari 2012). Some assumptions considered included continuous flow, no slip, and no temperature fluctuation at the walls. This model

was experimentally validated. It mainly served to help understand how humidity fluctuates while water vapor is continually produced and to understand the relation between humidity and thermal gradients (Shahsavari 2012).

A non-isothermal model of thermal effects based on two dimensional analysis was performed by Afshari and Jazayeri (Afshari 2006). They developed governing equations, derived from conservation equations, for the system and then solved them using finite element analysis. The model considered variations in fuel cell operating temperate which was varied between 333 K and 363 K (Afshari 2006). The authors found that the four most important parameters for a fuel cell is relative humidity, GDL thermal properties, fuel cell operating temperature, and the electrical conductivity (Afshari 2006). Reaction rate was calculated using the Butler-Volmer equation. The study concludes that temperature variation is more significant if current density is high. It was also shown that much of the heat is generated at the cathode, near the catalyst (Afshari 2006).

Meng and Wang developed a comprehensive three dimensional model on the functioning of a PEMFC (Meng 2004). This model considered heat transfer, electrochemistry, and water production. It was solved by applying boundary conditions to equations for conservation of mass, energy, and momentum. The model contained a five channel serpentine flow pattern. High and low humidity conditions were tested. Darcy's law was used to calculate the flow of water. The model was experimentally validated. They have shown that low humidity is detrimental to the smooth performance of the PEMFC; however, a good design can overcome low humidity (Meng 2004). Also, current density is dependent on humidity conditions. At low humidity conditions, current density increases with an increase in the amount of water content (Meng 2004).

Andreasen and Kaer performed a comprehensive dynamic study of temperature variation in a PEMFC operating at elevated temperatures (Andreasen 2009). Their research aims at developing techniques to overcome the disadvantages of operating a fuel cell at high temperatures. Simulation results were experimentally validated. The main assumptions of the model include constant heat flow and constant open circuit voltage (Andreasen 2009). The authors used thermodynamic principles to calculate the amount of heat energy produced. The simulation involved modeling the stack temperature at various locations and finding the stabilization points. High temperature was experimentally simulated by using an electrical heating device around the cell. Results from the study allowed for calculation of an optimal fuel cell operating temperature (Andreasen 2009).

Ju et al. studied the thermal effects of a PEM fuel cell, using a single-phase and non-isothermal model, under different design and operating conditions (Ju 2005). Their results show that GDL thermal conductivity strongly impacts membrane temperature and plays an important role in the coupled thermal and water management of PEM fuel cells (Ju 2005). To maintain good proton conductivity through the membrane, during low humidity conditions, efficient cooling through the gas channel ribs becomes critical (Ju 2005).

Strahl et al. developed a two-dimensional 100 W PEM FC model using COMSOL, based on energy, momentum, and water mass balance (Strahl 2011). A two-dimensional model was chosen for computational efficiency. The model was able to show control mechanisms for water and thermal management. It consisted of an open cathode with a cooling fan directly attached, removing heat by forced convection and providing oxygen to the cathode. Processes accounted for in the model include momentum transport,

convective mass transport, diffusive mass transport, water generation, electro-osmotic drag, heat generation, convective heat transfer, and conductive heat transfer. Experimental validation of the model was successful, allowing comprehensive study of water transport and thermal control mechanisms (Strahl 2011).

Sharifi et al. developed two mathematical models to describe steady-state and dynamic voltage-current characteristics (Sharifi Asl 2010). The static model considers activation loss, internal resistances, mass transport, and concentrated species. Both mathematical models correspond well with experimental data obtained from the same stack design. The models predict output voltage profiles, pressure dynamics, mass concentrations, flow rates, and stack temperature (Sharifi Asl 2010).

B. Compression

A unique cylindrical fuel cell design, with a goal of portable applications was built and tested by Lee et al. (Lee 2010). It incorporates helical flow channels and is completely cooled by free convection with the surrounding air. The design resulted in better clamping pressure distribution, which was simulated and experimentally verified using pressure sensitive film. This means that lower clamping pressure is needed to maintain 2 MPa over all contacting regions and to reduce contact resistance to an acceptable value. At 0.6 V (SHE), the current density of the cylindrical cell, 210 mA cm^{-2}, was 37% higher than that of a typical planar design. The cylindrical cell outperformed a planar cell of the same size. This design, however, lacks the ability to be stacked like a conventional fuel cell; thus, generating a higher power output may be an issue.

In order to optimize fuel cell clamping pressure, Zhang et al. used an approach that consisted of finding an experimental constitutive relation between contact resistance and clamping pressure (Zhang 2006). Then they obtained clamping pressure results from finite element analysis (FEA). Next, contact resistance based on the clamping pressure obtained from FEA combined with the constitutive relationship was predicted. Finally, they experimentally validated the predicted contact resistance.

The experimental setup used by Zhang et al. implemented a custom-made hydraulic press with a micro-ohmmeter (Zhang 2006). A GDL was sandwiched between two flat, non-featured bi-polar plates. This was then placed between two gold plates. From that setup, contact resistance can be tested at various levels of compression. The clamping pressure was varied from 0.5 to 3.0 MPa, compared to the typical clamping pressure of 1 MPa (Zhang 2006).

The constitutive relationship found by Zhang et al. was solved using the least squares method (Zhang 2006). Data was obtained by taking 15 experimental values at varying clamping pressures ranging from 0.5 MPa to 4.8 MPa (Zhang 2006). It was found that increasing clamping pressure has less effect on contact resistance at higher values (Zhang 2006). So the clamping pressure should be set to a point where contact resistance won't benefit much from an increase but, also where the gas flow is not being obstructed and no materials incur damage.

Zhou et al. explored the effects of porosity change due to compression in order to find a nominal clamping pressure (Zhou 2007). Zhou et al. was able to perform FEA on the GDL and determine its deformation (Zhou 2007). From there, the deformation and porosity information was implemented into another simulation to determine a

polarization curve. This allowed them to find the effect clamping pressure has on performance of a fuel cell. The second simulation used several assumptions (steady flow state, isothermal flow, etc.) and modern analysis techniques; Darcy's law, Butler-Volmer equations, etc. (Zhou 2007). Using this data and performing several iterations at different clamping pressures; an optimum clamping pressure of 1.93 MPa on the GDL was determined (Zhou 2007).

R. Montaini et al. tested a 25 cm^2 single cell PEMFC to investigate the effect of endplate stiffness on pressure distribution (Montanini 2011). A correlation between the pressure distribution on the MEA and clamping torque was also assessed. The fuel cell consisted of aluminum endplates, copper current collectors, carbon paper GDLs, Nafion membranes, and PTFE gaskets (Montanini 2011). The assembly was clamped together with eight bolts (corners and middles) at 5 to 10 N·m in 1 N·m increments (Montanini 2011). To examine contact pressure experimentally, a digital piezoresistive sensor was placed between the MEA and graphite plate. Endplate out of plane deformation was measured using an optical full-field measurement technique (Montanini 2011). A clamping torque of 5 to 10 N·m corresponds to an average pressure of 836 kPa to 1049 kPa on the MEA, as found by R. Montaini et al. (Montanini 2011). The gasket increased to 17.7 MPa at 10 N·m with peaks above 20.7 MPa (Montanini 2011). Clamping pressure distribution is dependent on bolt configuration. Because of how a fuel cell functions, the bolts are limited in their position. This results in a curvature of the endplates which is thought to be strictly related to MEA pressure distribution. The average pressure on the MEA increased by 25% while the gasket pressure increased by 64% (Montanini 2011). This shows that the gasket mainly supports

the clamping pressure and is a direct result of the different Young's modulus between materials. A suggestion was made to use pre-curved endplates.

To study the effects of clamping pressure on the electrochemical performance of a fuel cell Chang et al. started by determining the electro-physical properties of the GDL which include electrical resistance, porosity, and gas permeability (Chang 2007). To do this, a test stand was built incorporating a milliohm meter and thickness gauge. The test stand consisted of copper ends that apply the pressure and a GDL (carbon paper) sandwiched between featureless carbon plates. Various clamping pressures were applied and the resulting assembly resistance calculated via the Ohm's law equation (Chang 2007). In order to extrapolate the interfacial resistance between GDL and carbon plate; testing was done without the GDL. For this a double thick layer of carbon was used in order to maintain the correct resistance and avoid adding the interfacial resistance between two carbon plates (Chang 2007). So, all interfacial resistances are known except for that between the GDL and carbon plate, which can be deduced.

When using carbon cloth as a GDL, Lin et al. found that increasing pressure caused interlocking of the carbon fibers which decreased through-plane resistance (Lin 2008). Excessive compression damages the carbon fibers reducing electrical conductivity. Compression influences porosity, thickness, and electrical resistance. Lin et al. implemented low compressibility gaskets of various thicknesses to dictate the compression of the GDL (Lin 2008). By doing this, a performance graph was obtained at various GDL compressions which enable optimization of the stack. The study resulted in an optimum compression ratio (operating thickness compared to original thickness) of about 60% with carbon cloth (Lin 2008).

In order to optimize rib shape of the gas channels, Zhou et al. first obtained the optimum contact pressure and from that the optimum rib shape. Using a finite element method, a contact resistance model was developed (Zhou 2006). In plane deformation has relatively insignificant effects and was neglected. Taking into account effects of porosity and contact resistance, an optimum shape can be determined. It was found that a semi-circular rib, as opposed to a flat rectangle, is the best design for minimizing contact resistance and to give a uniform distribution of contact pressure (Zhou 2006).

According to Avasarala and Haldar, the interfacial contact resistance between bi-polar plate and GDL is largely dependent on their surface topology or roughness (Avasarala 2009). The actual contacting surface area decreases as the roughness of the surface increases (Avasarala 2009). The experiment included several examples of composite bi-polar plates and various grit sizes of sandpaper to smooth the surface. Unpolished plates can contain a non-conductive, polymer rich layer on its surface (Avasarala 2009). The results of the study show that, while smoothing the surface can certainly decrease contact resistance, the benefits are dependent on materials and stack design (Avasarala 2009). Monitoring of the bi-polar plate surface topology must be performed when choosing a polishing method.

Wen et al. performed testing with a pressure sensitive film on a single cell and 10-cell stack in order to find the optimum bolt configuration and clamping pressure (Wen 2009). Bolt configuration is varied by their positions and number used. It is found that a 6-bolt configuration worked best for the rectangular 100 cm^2 active area configuration (Wen 2009). Compression simulations showed the maximum safe clamping torque is 16 N·m and this torque ultimately resulted in the best performance (Wen 2009).

Decreases in porosity of the GDL did not appear to have a significant effect in the 10-cell stack (Wen 2009). Increasing clamping pressure improved pressure distribution, however; maximum power did not increase monotonically (Wen 2009). It appears that cell to cell variations mean local pressure distributions have an important influence.

Yu et al. attempted to solve the problem of proper stack compression by using carbon fiber and glass fiber reinforced composite end-plates with pre-curvature due to residual heating (Yu 2010). Pressure sensitive films were used to experimentally test the pressure distribution. The goal of this study was to correct the low pressure area in the middle of the stack under traditional loading (Yu 2010). It was found that the pre-curved plates provide a more uniform pressure distribution and decrease weight compared to conventional steel end plates (Yu 2010).

In order to determine what effect dimensional error in manufacturing the bipolar plate has on GDL pressure distribution; Liu et al. performed FEA and Monte Carlo simulation with randomly varying channel rib heights (Liu 2009). With this information a regression equation was calculated to represent the relationship between GDL pressure distribution and dimensional error. This allowed Liu et al. to determine the maximum allowed dimensional error in the manufacturing of metallic bipolar plates (Liu 2009). This study focused on metallic bipolar plates because of their electrical and mechanical properties as well as their affordability and ease of manufacturing (Liu 2009). The study concludes that the relationship found is acceptable to determine the maximum dimensional error allowed (Liu 2009). A maximum dimensional tolerance of 0.5 ± 0.015 mm was determined for the metallic bipolar plate used in the study (Liu 2009).

Tan et al. have estimated the relationship between torque applied and the functioning of the gasket in a PEMFC using pressure sensitive film (Tan 2007). Finite element analysis was used to obtain the exact correlation between stress and deformations produced after the gasket had been subjected to loading. A comprehensive model was developed which correlated the applied loading to the deformation in the gasket and end plates (Tan 2007).

Wang et al. considered the significance of having uniform pressure across the GDL and MEA in a PEM fuel cell (Wang 2004). To optimize pressure distribution they designed and developed specially pressurized endplates for testing. The novelty in the endplates was a pocket of hydraulic fluid pressing against the fuel cells (Wang 2004). Pressure sensitive film was used to examine magnitude and distribution transmitted by the hydraulically driven end plates. Also the authors studied the effect of different gasket sizes and developed a comprehensive FEM model for pressure distribution in the fuel cell (Wang 2004).

Ihonen et al. developed a new fuel cell design that is capable of measuring clamping pressure and electrical contact resistance at the same time (Ihonen 2001). The researchers developed MEAs of various thicknesses using thin film technology with a Nafion base and platinum catalyst (Ihonen 2001). The novel cell design consisted of stainless steel current collectors plated with platinum to improve their efficiency. Electrochemical data was collected for a commercial fuel cell and compared against the novel cell. Based on their studies, the researchers were able to show that stainless steel is not a good material because of its' high and unstable contact resistance; however, this problem was solved by using a platinum or chromium coating on the stainless steel (Ihonen 2001). This method

provides a good technique to measure in-situ contact resistance and clamping pressure in the fuel cell simultaneously (Ihonen 2001).

III. INSTRUMENTATION AND EQUIPMENT

A Carver bench top standard auto press was used for compression testing. The Carver press allows for a continuous, set loading to be applied for a specified amount of time. Fuel cell performance was tested using Arbin Instruments fuel cell testing equipment. The fuel cell testing equipment allows for the control of reactant gas flow rates and fuel cell operating parameters.

IV. EXPERIMENTAL PROCEDURE

A. Fuel Cell Performance Testing

Fuel cell performance was tested for a single cell using fuel cell testing equipment. The fuel cell testing equipment allows for control and recording of the hydrogen flow rate, voltage, and current of the fuel cell. The fuel cell testing equipment also contains a hydrogen sensor that can detect hydrogen gas leakage.

B. Compression Testing

Experimental testing of the clamping pressure involves placing pressure sensitive film in specific locations throughout the stack. The pressure sensitive film has a range of 0 to 2.5 MPa. When pressure is applied to the film it changes colors from white to red via bursting microcapsules. Pressure is approximated depending on the density of red spots in the film. The effects of load on GDL thickness were tested by placing a GDL of known thickness in a hydraulic press under various pressures and for a set amount of time, then measuring the resulting thickness.

Clamping of the fuel cell stack was done using a torque wrench to apply a known torque. From simulation and previous research, it was known that the center of the GDL has very low pressure. To correct this, center pins were placed in the center region of the endplate. These pins apply pressure directly to the conduction plate which in turn, applies more pressure to the center of the GDLs. Because we were unable to use a torque wrench on these small pins; a specific loading was applied to the center region of the stack using a hydraulic press. To accomplish this, wooden blocks were placed in the center region of

the endplate. The wooden blocks extended past the bolts so that the hydraulic press only came into contact with the wood.

Two types of GDLs were used: uncoated carbon paper and Nafion (perfluorinated ion-exchange polymer) coated carbon paper (Avcarb GDS2120). The coated GDLs have a thickness of 0.22 mm whereas the non-coated GDLs have a thickness of 0.14 mm.

To identify pressure-sensitive film location, cells were labeled 1 through 16 with 1 being the cell nearest the anode endplate. Application of the loading on a 16-cell stack was done using four different clamping pressure methods. For method one eight pressure sensitive films were inserted between the bipolar plate and GDL of cells 1-8. Coated GDLs were used. A torque of 10.17 N·m (90 lb·in) was applied to the bolts and a force of 11.12 kN (2500 lb) was applied by the hydraulic press for 10 minutes. For method two, eight pressure sensitive films were inserted between the bipolar plate and GDL of cells 1-8. Coated GDLs were used. A torque of 10.17 N·m was applied to the bolts first. Then a 59.16 N (13.3 lb) weight was placed on the center region of an endplate and left alone for three days. Last, the stack was placed in the hydraulic press with an applied load of 11.12 kN for 10 minutes. For method three, pressure sensitive film was placed in all 16 cells of the stack. In cells 1-8, pressure sensitive film was placed between bipolar plate and coated GDL. In cells 9-16, pressure sensitive film was placed between bipolar plate and non-coated GDL. A torque of 10.17 N·m was applied to the bolts and a force of 15.57 kN (3500 lb) was applied by the hydraulic press for 10 minutes. Finally for method four pressure sensitive film placement was identical to method three. A torque of 10.17 N·m was applied to the bolts first. Then a 59.16 N weight was placed on the center region of

an endplate and left alone for three days. Last, the stack was placed in the hydraulic press with an applied load of 15.57 kN for 2 hours.

V. SIMULATION SETUP

The analysis of species transport in a PEM fuel cell is complicated by several factors. The species always exist as a complex mixture, because liquid water is present in both the anode side and the cathode side of the fuel cell. Gases must flow through the porous gas diffusion layer (GDL) and the electrode/catalyst layer, which is generally difficult to compute. Also, the transport of ions through the membrane must be considered along with back diffusion of water from the cathode to the anode. The following sections will describe the equations and assumptions used to analyze species transport, electrochemical effects, and heat transfer in a PEM fuel cell. Simulations were performed using the program COMSOL which implements MUMPS (MUltifrontal Massively Parallel sparse direct Solver). MUMPS solves large linear systems with parallel factorization, iterative refinement, and backward error analysis. All coupled equations are solved simultaneously until the convergence is obtained.

A. Model Setup

Several different fuel cell configurations were simulated using COMSOL. The first configuration is shown in Figure 1. This configuration was experimentally tested. The remaining configurations were simulated to show the programs ability to evaluate different flow fields and flow plate designs. The configuration shown in Figure 1 has an active area of 31.5 cm^2. The active area refers to the region of the fuel cell where reaction can take place. Channel width was 1.5 mm, channel depth 0.5 mm, and channel separation was 1.0 mm. Two GDLs were tested experimentally.

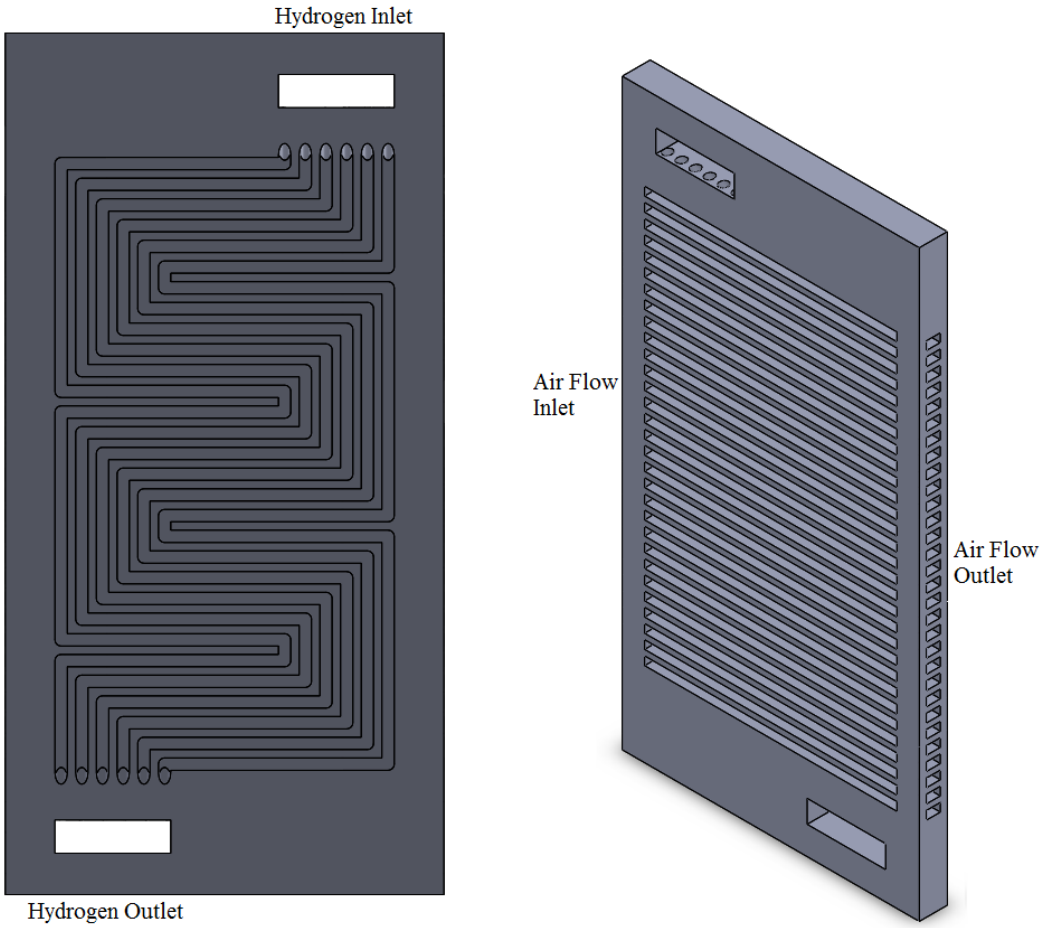

FIGURE 1 – Experimentally Tested 35 cm^2 Active Area Rectangular Fuel Cell

The cell shown in Figure 1 is an open cathode design. The flow rates used in simulation were 0.50 L/min for hydrogen and 2.5 L/min for air.

For the remaining configurations simulated; Table 1 lists the critical dimensions of the fuel cells studied and assigns each a “case” number.

TABLE I

PEM FUEL CELL DIMENSIONS FOR THREE CASES

Dimension	Case 1	Case 2	Case 3
Channel Width (mm)	1.1	1.1	1.1
Channel Depth (mm)	1.62	1.62	1.62
Channel Separation (mm)	0.9	0.9	0.9
Active Area (cm^2)	100	200	200
GDL Thickness (mm)	0.25	0.25	0.25
Electrolyte Layer Thickness (mm)	0.1	0.1	0.1

Figure 2(a-f) shows the channel design and cooling design for each case.

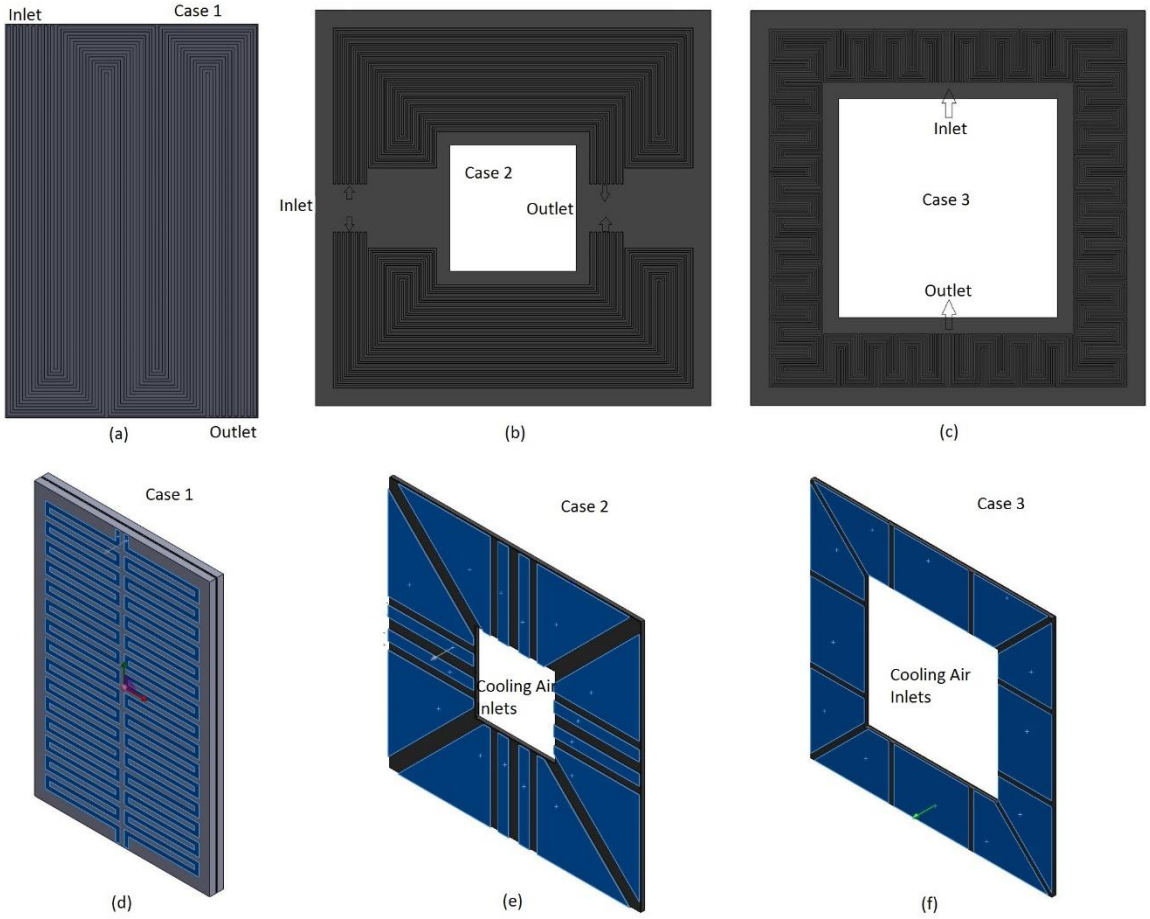

FIGURE 2 - Case 1, (a) Channel Design for 100 cm^2 Active-Area Rectangular Fuel Cell; Case 1, (b) Channel Design for 200 cm^2 Active-Area Square Fuel Cell with Small Bend Number; Case 2, (c) Channel Design for 200 cm^2 Active-Area Square Fuel Cell with High Bend Number; Case 3, (d) Channel Design for Water Cooling in Case 1, (e) Air Cooling Pattern for Case 2, And (f) Air Cooling Patter for Case 3 (in d, e, and f, the Highlighted Region Represents the Cooling Fluid Volume)

A Maxwell-Stefan model is adopted for convection and diffusion. Momentum transfer is modeled by the Navier-Stokes equations. Brinkman equations model flow through the porous layers and electrochemical effects are modeled using Ohm's law in conjunction with the Butler-Volmer equation. Fluid flow is considered to be compressible and laminar. Input parameters necessary for simulation are listed in Table 2.

TABLE II

FUEL CELL MODEL PARAMETERS

Value	Description	Reference
0.4	GDL porosity	(Bernardi and Verbrugge 1992)
$1.18x10^{-11}$ [m^2]	GDL permeability	(Feser, Prasad et al. 2006)
222 [S m^{-1}]	GDL electric conductivity	(Nitta, Hottinen et al. 2007)
0.743	Inlet H_2 mass fraction	(Yilanci, Dincer et al. 2008)
0.023	Inlet H_2O mass fraction	(Yilanci, Dincer et al. 2008)
0.228	Inlet oxygen mass fraction	(Yilanci, Dincer et al. 2008)
40.88 [mol m^{-3}]	Oxygen reference concentration	(Wu, Li et al. 2007)
40.88 [mol m^{-3}]	Hydrogen reference concentration	(Wu, Li et al. 2007)
9.825 [S m^{-1}]	Membrane conductivity	(Zhang, Désilets et al. 2011)
$1.19x10^{-5}$ [Pa s]	Anode viscosity	(Ramesh, Dimble et al. 2011)
$2.46x10^{-5}$ [Pa s]	Cathode viscosity	(Ramesh, Dimble et al. 2011)
838 [J kg^{-1} K^{-1}]	Membrane heat capacity	(Jiao and Li 2010)
0.254 [W m^{-1} K^{-1}]	Membrane thermal conductivity	(Burheim, Vie et al. 2010)
0.02 [kg mol^{-1}]	Hydrogen molar mass	
0.028 [kg mol^{-1}]	Nitrogen molar mass	
0.018 [kg mol^{-1}]	Water molar mass	
0.032 [kg mol^{-1}]	Oxygen molar mass	
$101x10^3$ [Pa]	Reference pressure	
0.6	Cell voltage (V_cell)	
333 [K]	Initial cell temperature, fluid injection temperature (T)	

The setup described above is applied to all four simulation configurations. The only differences are between the active area, flow channel pattern, and cooling design. Case 1 is the more traditional rectangular design with an active area of 100 cm^2, shown in Figure

2(a). Case 1 is simulated twice, once without any cooling and once with water cooling. Case 2 has an active area of 200 cm^2 and a large hole in the center for better temperature distribution and forced air convection; it is shown in Figure 2(b). Case 3, Figure 2(c), also has an active area of 200 cm^2; however, it is wider, and the channel design has an increased number of turns. The areas highlighted in Figure 2(d) represent the water cooling channels in case 1 of the simulations. Figure 2(e) displays the areas where cooling air for case 2 will travel from the center hole and out through the cell. The same concept is implemented into case 3, shown in Figure 2(f). Fluid flow volumes are represented as solid objects for the simulations.

B. Current Distribution

Ohm's law is used to solve for the electronic and ionic potential of the cell:

$$i_l = -\sigma_l \nabla \phi_l \qquad i_s = -\sigma_s \nabla \phi_s \tag{4}$$

All model domains are included except for the anode and cathode flow channel volumes which are occupied by reactant gas. Local current density depends on reactant concentrations which must be pulled from the two transport of concentrated species physics modules.

The anode side GDL, anode side electrode, and electrolyte have initial values set to 0 V (SHE) for electrolyte and electric potential. Initial values of the cathode side are set with the electrolyte potential at 0 V (SHE) and the electric potential at V_cell, a variable set to 0.6 V (SHE) for the simulated images presented. The anode electrode is defined as a porous electrode and uses the linearized Butler-Volmer equation to find current density:

$$i_{loc} = i_0 \left(\frac{n\mathrm{F}}{RT}\right)\eta \tag{5}$$

Equation (5) is the equation used to calculate activation overvoltage in "Fuel Cell Fundamentals" (O'Hayre, Cha et al. 2006). The term i_0 is the exchange current density determined by the equation:

$$i_0 = \left(\frac{chcs.c\_wH2}{cH2\_ref}\right)^{0.5} \tag{6}$$

The cathode electrode is also defined as a porous electrode; however, the cathodic Tafel equation

$$\eta = \frac{RT}{\alpha n\mathrm{F}} \log\left(\frac{-i_{loc}}{i_0}\right) \tag{7}$$

is used to find current density. This is the more general and common representation of the exchange current density at an electrode. The general representation can be obtained from Larminie and Dicks in the form $\Delta V_{act} = A * \ln (i/i_0)$ (Larminie 2006). Even though the temperature is not constant, the tafel equation at low current densities on a single electrode (anode or cathode) can be represented in the form $\Delta V = A\ ln\ (i/i_0)$ where 'i_o' is the exchange current density and 'i' is just the current density. The term ΔV_{act} represents the overpotential and A is the cathodic tafel slope (depends on the cathode material). This is considered at an ambient temperature condition of 298K. The exchange current density is defined by the equation:

$$i_0 = \frac{chcs2.c\_wO2}{cO2\_ref} \quad (8)$$

The equilibrium reference potential, derived from the Nernst equation, for the cathode electrode is set to 1.15 V (SHE). With the equilibrium reference potential, $E_{0,eq}$, the equilibrium potential, E_{eq}, based on temperature is determined using $E_{eq}=E_{0,eq}+dE_{eq}/dT(T-T_{ref})$. The equilibrium potential is then used together with $\mu=\varphi_s-\varphi_l-E_{eq}$, Equation (7), and Equation (8) to back out the local current density. Finally, the anode GDL is defined as the electric ground, while the cathode GDL is set with an electric potential of 0.6 V (SHE).

C. Transport of Concentrated Species

This module solves for the concentration of each species throughout the fuel cell. A Maxwell-Stefan diffusion model is used and the anode and cathode sides are separated by two transport of concentrated species modules to improve calculation time. Convection is also considered in this module. The dependent variables are the mass fractions of hydrogen and water in the anode side and the mass fractions of oxygen, nitrogen, and water in the cathode side. All domains, except the electrolyte, are included in this module, with anode side components in one and cathode side components in the other.

Convection and diffusion through the channel, GDL, and electrode are modeled in this module using the Maxwell-Stefan diffusivity matrix. Vural et al. discussed various mass transfer models and showed that the Maxwell-Stefan model is very well suited to handle fuel cell dynamics (Vural 2010). Velocity ($\boldsymbol{u}$) and pressure are pulled from the Free and Porous Media Flow module. The overriding equation is the following:

$$\nabla \cdot \boldsymbol{j}_i + \rho(\boldsymbol{u} \cdot \nabla)\omega_i = R_i \tag{9}$$

The density (ρ) is solved using the ideal gas equation. R_i is a product of the number of participating electrons and the stoichiometric coefficient:

$$R_i = \frac{\nu_i i_{loc}}{nF} \tag{10}$$

In the anode electrode, the number of participating electrons is set to two and the stoichiometric coefficient of hydrogen is one. The cathode side uses an almost identical setup; however, we are dealing with three species instead of two: oxygen, water, and nitrogen. For the two-phase mixture in the gas channel, the Maxwell-Stefan mass transport equation was used

$$F_i = \sum_{i \neq j} \zeta_{i,j} x_j (u_i - u_j) \tag{11}$$

where, F_i is the driving force on i, at a given T and p, $\zeta_{i,j}$ is the friction coefficient between i and j; x_j is mole fraction of j, and u is velocity. For the multiphase mixture flow in the GDL, Darcy's Law was used for momentum transport modeling:

$$\frac{\partial(\rho \boldsymbol{u})}{\partial t} + \nabla \cdot (\rho \boldsymbol{u}^2) = -\nabla \boldsymbol{P} + \nabla \cdot (\nabla \mu \boldsymbol{u}) - \frac{\mu}{K}(\varepsilon \boldsymbol{u}) \tag{12}$$

The species conservation equation for the multiphase mixture is

$$\varepsilon \frac{\partial}{\partial t}(\rho C^{\alpha}) + \nabla \cdot (\gamma_{\alpha} \rho \boldsymbol{u} C^{\alpha}) = \nabla \cdot (\varepsilon \rho D \nabla C^{\alpha}) + \nabla \cdot [\varepsilon \sum_k \rho_k s_k D_k^{\alpha} (\nabla C_k^{\alpha} - \nabla C^{\alpha})] - \nabla \cdot [\sum_k C_k^{\alpha} j_k] \quad (13)$$

Boundary and initial conditions at the interface between the membrane and the cathode are:

$$u(x = 0) = u_{in} \qquad v(x = 0) = 0 \quad (14)$$

$$\frac{\partial C^{H_2}}{\partial x}(x = L) = C_{in}^{H_2} \quad (15)$$

$$C^{H_2O}(x = L) = \frac{\rho_{g,sat}^{H_2O} RH_{in}^{H_2}}{\rho_g} \quad (16)$$

D. Free and Porous Media Flow

The Free and Porous Media Flow module describes the flow of the chemical species through the channels, GDLs, electrodes, and electrolyte. It incorporates the Navier-Stokes equations for the flow channels and Brinkman equations for the porous layers. Laminar flow conditions control the inlets and outlets of both hydrogen flow and air flow. All walls use a no-slip boundary condition, keeping fluid velocity at the walls at zero.

The dependent variables for this module are the velocity field and pressure. The overriding equations include:

$$\rho(\boldsymbol{u} \cdot \nabla)\boldsymbol{u} = \nabla \cdot \left[-\boldsymbol{P}l + \mu(\nabla \boldsymbol{u} + (\nabla \boldsymbol{u})^T) - \frac{2}{3}\mu(\nabla \cdot \boldsymbol{u})l\right] + F \quad (17)$$

$$\nabla \cdot (\rho \boldsymbol{u}) = 0 \tag{18}$$

$$\frac{\rho}{\varepsilon_p}\left((\boldsymbol{u}\cdot\nabla)\frac{\boldsymbol{u}}{\varepsilon_p}\right) = \nabla\cdot\left[-\boldsymbol{P}l + \frac{\mu}{\varepsilon_p}(\nabla\boldsymbol{u} + (\nabla\boldsymbol{u})^T) - \frac{2\mu}{3\varepsilon_p}(\nabla\cdot\boldsymbol{u})l\right] - \left(\frac{\mu}{K_{br}} + \beta_F|\boldsymbol{u}| + Q_{br}\right)\boldsymbol{u} + F \tag{19}$$

The flow is considered as compressible flow. The density, ρ, is pulled from the Transport of Concentrated Species modules. Karimi and Li describe the use of Navier-Stokes and Brinkman equations in fuel cell analysis (Karimi 2005). The inlets are governed by laminar flow with an established input flow rate. Outer edges are constrained to zero. The outlets are also governed by laminar flow, with the exit pressure set to ambient. The flow through porous materials is linked to electrochemical effects by a Porous Electrode Coupling. This provides the molar mass of each species, to be used in solving flow in the porous materials.

E. Heat Transfer

The effects of heat transfer are very important in a fuel cell study. Temperature affects almost every aspect of the fuel cell performance, from diffusivity to reaction rate. Heat transfer is simulated for case 1; without water cooling and with water cooling. The dependent variable is, of course, temperature. The overriding equation is given as:

$$\rho C_p \boldsymbol{u}\cdot\nabla T = \nabla\cdot(k\nabla T) + Q \tag{20}$$

Most of the heat produced by a fuel cell is a by-product of the electrochemical reaction and is implemented into the simulation via the equation:

$$-\boldsymbol{n} \cdot (-k\nabla T) = Q_b \tag{21}$$

This value is carried over from the Secondary Current Distribution module. A separate node is applied to both anode and cathode to represent both half reactions individually.

Joule heating is another source of heat in a fuel cell. This is a result of each material's resistance while a current flows through it. The resistance causes heating and is described by Equation (21). In this case, Q is total power dissipation density, and it is also brought in from the Secondary Current Distribution module.

Heat dissipation results from surface-to-ambient radiation and convection, convection from gas flow out of the cell, and water or air cooling. For both cases, surface-to-ambient heat transfer hardly contributes to cooling, as it is only applied to the edges of the bipolar plate material. Inlet fluid temperatures and initial cell temperature are set to 333 K for all cases.

F. Compression

The single cell model to be simulated includes the following components; two end-plates, two bi-polar plates, two GDLs, two gaskets and, an MEA. The GDL and gasket comprise one layer of the fuel cell with the GDL sitting inside the gasket. Material properties are applied to each component as shown in Table III. The values are taken from data sheets, when available, of the materials that are to be used in the experimental study. Poisson's ratio of the GDL was taken from a study by Zhang et al. (Zhang 2006).

The bipolar plate Poisson's ratio is from a study by Lee et al. which evaluated electrical, mechanical, and molding properties of a composite graphite bipolar plate (Lee 2007). The Nafion membrane Poisson's ratio comes from a study by Li et al. on ionic clustering in Nafion (Li 2000). The dimensions of each component are also shown in Table III. The head and nut diameter are both 15.405 mm and the bolt holes themselves are 10.27 mm. It is a standard nut and bolt configuration. All features have been removed from the materials except for gas channels in the bi-polar plates. The channel dimensions are shown in Table IV.

TABLE III

MATERIALS AND PROPERTIES FOR COMPRESSION SIMULATION

Layer	End-plate	Bi-polar plate	GDL	Gasket	PEM
Material	Stainless steel	Carbon graphite	Carbon paper	Silicon	Nafion
Density (kg m^{-3})	7,800	2,240	480	2,330	918
Poisson's ratio	0.28	0.29	0.33	0.30	0.33
Elastic modulus ($N \cdot m^{-2}$)	2e11	6.865e11	5.634e7	5.394e8	1.814e7
Dimensions (mm)	234x149	195x109	133x84	195x109	195x109
Thickness (mm)	12.7	3.175	0.254	0.220	0.100

TABLE IV

DIMENSIONS FOR 100 CM^2 ACTIVE AREA BI-POLAR PLATE

Dimension	**Value**
Channel Width	1.1 mm
Channel Depth	1.62 mm
Active Area	25 cm^2
GDL Thickness	0.38 mm
Electrode Layer Thickness	0.05 mm
Electrolyte Layer Thickness	0.1 Mm

All components are modeled as 3D objects and keep their general form. A no penetration constraint is applied to keep the materials from moving into each other's space. An inertial relief setting is also used. This keeps the model from moving off in space from the forces exerted since the FC is not physically fixed to any solid non-moving object. The goal is to have as realistic a simulation as possible with the current tools available.

VI. RESULTS AND DISCUSSION OF RESULTS

A. Transport, Electrochemical, and Heat Transfer

1. Simulation and experimentation of 31.5 cm^2 cell with air cooling

The cell configuration shown in Figure 1 has an active area of 31.5 cm^2 with cell dimensions given in the model setup section of this thesis. This cell was simulated using a parametric solver to vary the voltage drawn from the cell. The external voltage used in simulation varied from 0.4 to 0.9 V with an increment of 0.05 V. The resulting polarization curve is shown in Figure 3.

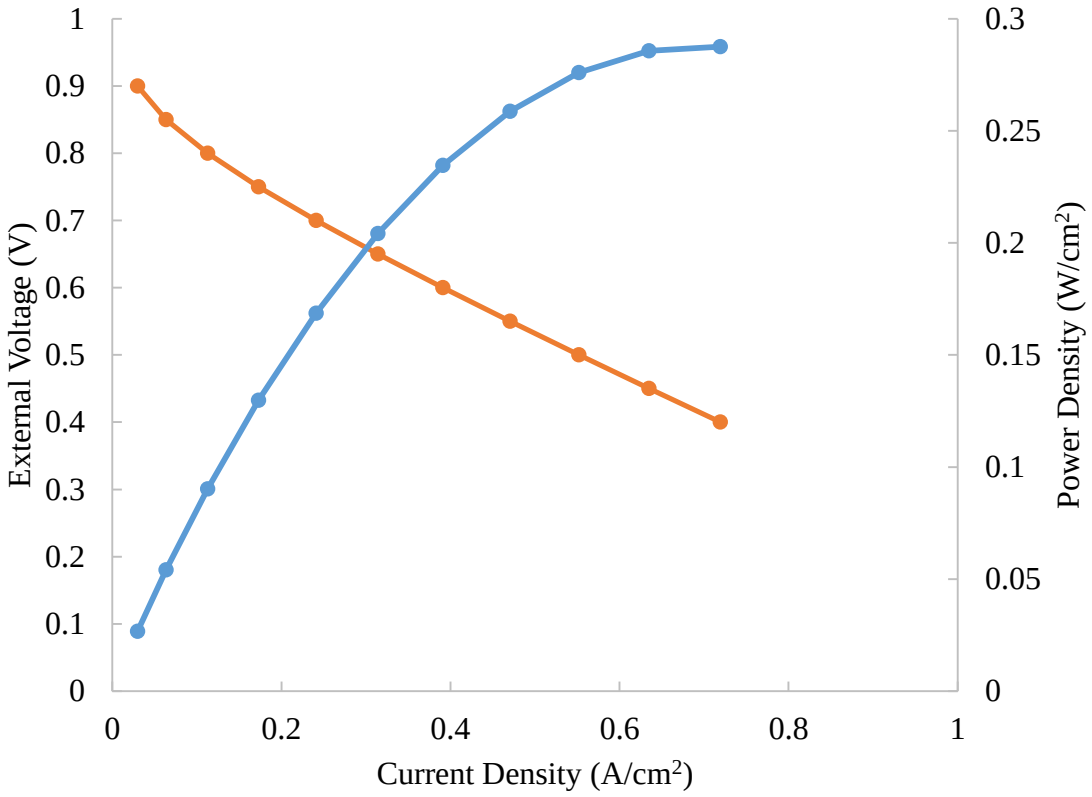

FIGURE 3 – Polarization Curve for a 31.5 cm^2 Active Area, Single Cell Fuel Cell

The polarization curve shows a maximum power density of 0.287 W cm^{-2} at a voltage of 0.4 V and current density of 0.719 A/cm^2. The peak power output of the cell for the given active area was 9.05 W. The results of this simulation in terms of species transport and heat transfer is shown in Figure 4.

The hydrogen mass fraction shown in Figure 4(a) enters the flow plate at a maximum mass fraction of 0.743 and exits at a mass fraction of 0.32. There is a large gradient in hydrogen mass fraction across the channels of this flow plate. Oxygen mass fraction is shown in Figure 4(b) entering the cell at 0.23 and exiting the cell only slightly reduced. This is because air is supplied at a high flow rate in order to deliver sufficient oxygen to the cell as well as maintain the cells temperature. Oxygen mass fraction is as low as 0.15 in the GDL as it takes time for oxygen to diffuse and it is continually being used up.

The mass fraction of water produced in the cathode is shown in Figure 4(d). At the cell inlet the water mass fraction is 0.023 and it increases slightly toward the exit. The water mass fraction is highest in the GDL with a value of 0.107. Water is produced in the GDL and will either back diffuse through the MEA or travel out of the cathode flow plate channels and out of the fuel cell. Figure 4(c) shows the temperature variation on the carbon composite material of the bipolar plate. In this simulation hydrogen and air enter the cell at 293 K, room temperature. Air flow through the cathode flow channels provides cooling to the fuel cell. Due to electrochemical effects and resistive heating the cell temperature reaches almost 300 K near the hydrogen and air exit.

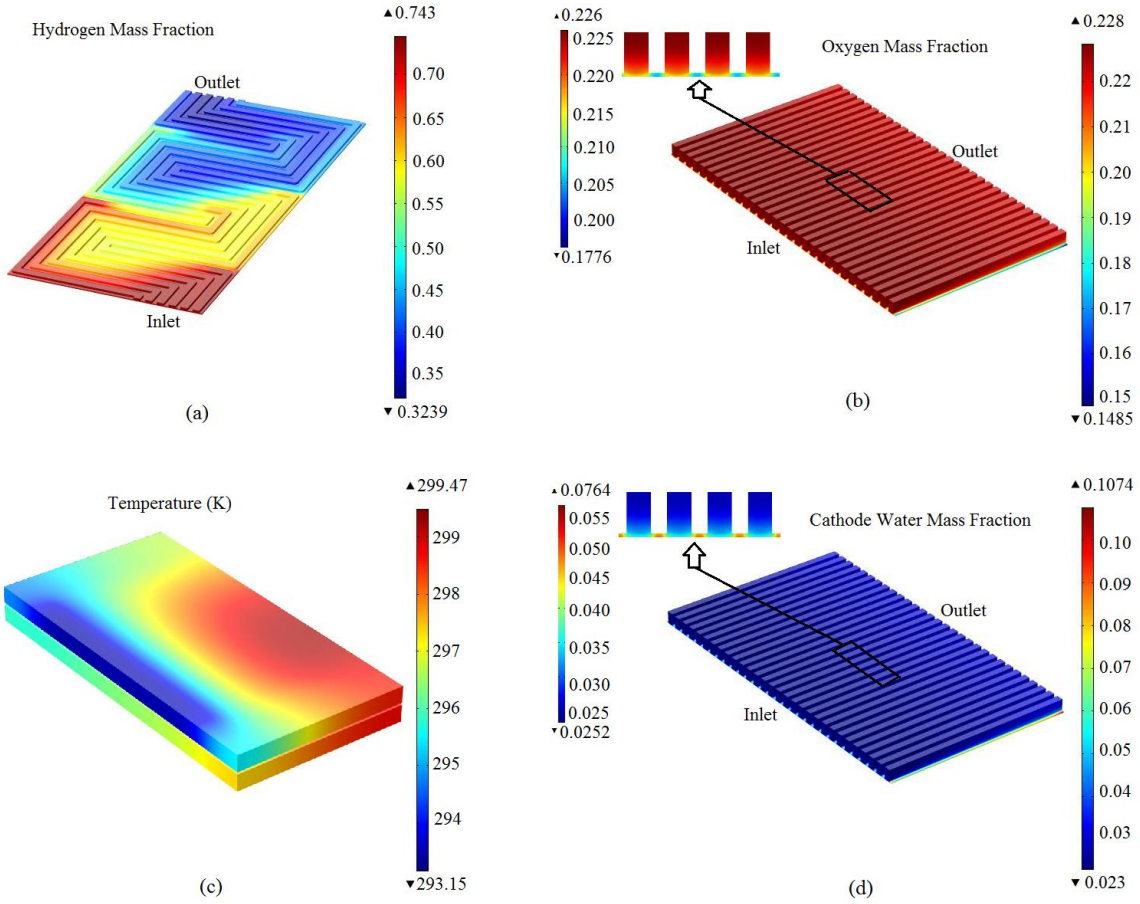

FIGURE 4 – Open Cathode, 31.5 cm^2 Active Area (a) Hydrogen Mass Fraction Profile, (b) Oxygen Mass Fraction Profile, (c) Temperature Profile of the Cathode Side Bipolar Plate, and (d) Water Mass Fraction in the Cathode Channels, (Cell Voltage: 0.4 V)

The flow plate design shown in Figure 1 was tested experimentally. The fuel cell is shown in Figure 5 connected to the Arbin fuel cell testing equipment. The resulting polarization curve for the high performance MEA is shown in Figure 6. The high performance MEA is thinner and has a higher platinum loading leading to improved fuel cell performance. The polarization curve resulting from the high durability MEA is shown in Figure 7. The high durability MEA is much more robust and can withstand higher compression forces. When testing fuel cells, they are continually assembled and disassembled which makes a more robust MEA desirable. MEAs were tested under the same conditions; 0.5 LPM hydrogen flow rate and air flow provided by an external fan.

Both MEAs were optimized by the manufacturer for peak performance under standard room temperatures and humidity.

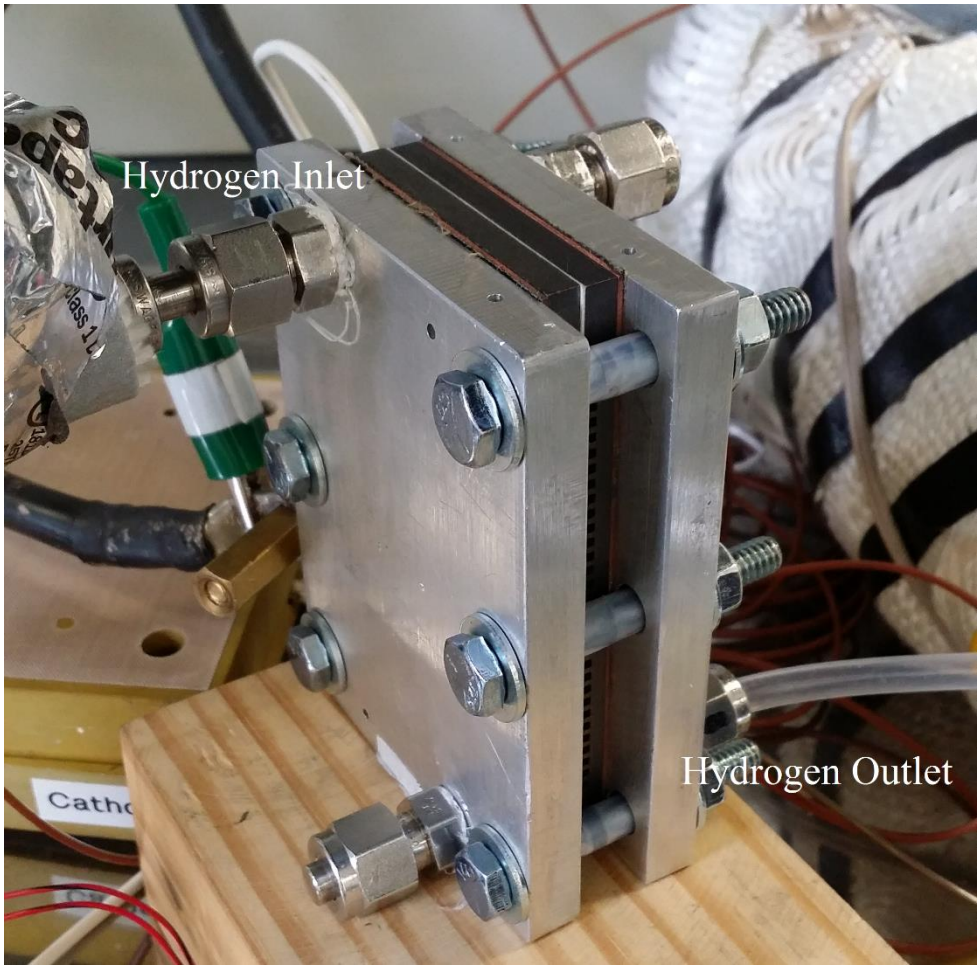

FIGURE 5 – Fuel Cell Connected to Arbin Testing Equipment

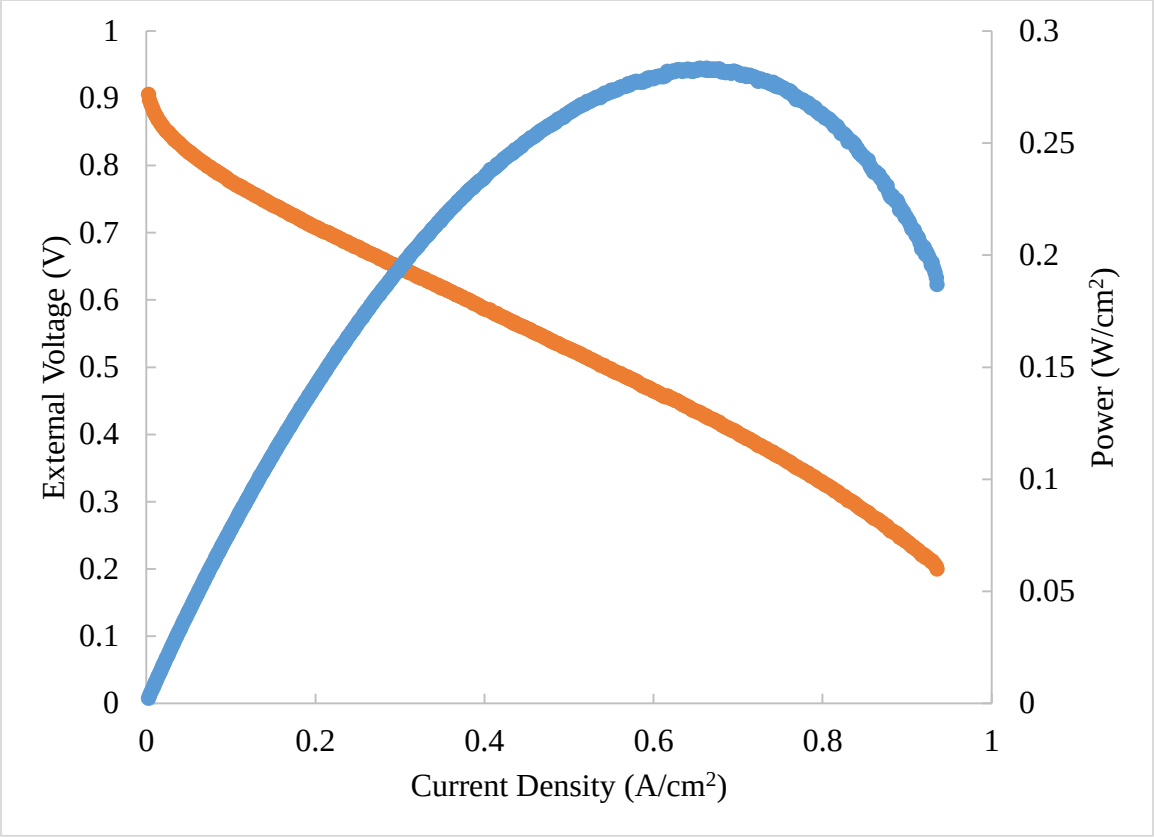

FIGURE 6 – Experimentally Tested Fuel Cell Polarization Curve Using a High Performance MEA

The maximum power density of the high performance MEA was 0.282 W/cm^2 at a cell voltage of 0.406 V and a current density of 0.695 A/cm^2. The peak power output of the fuel cell for a 31.5 cm^2 active area was 8.88 W.

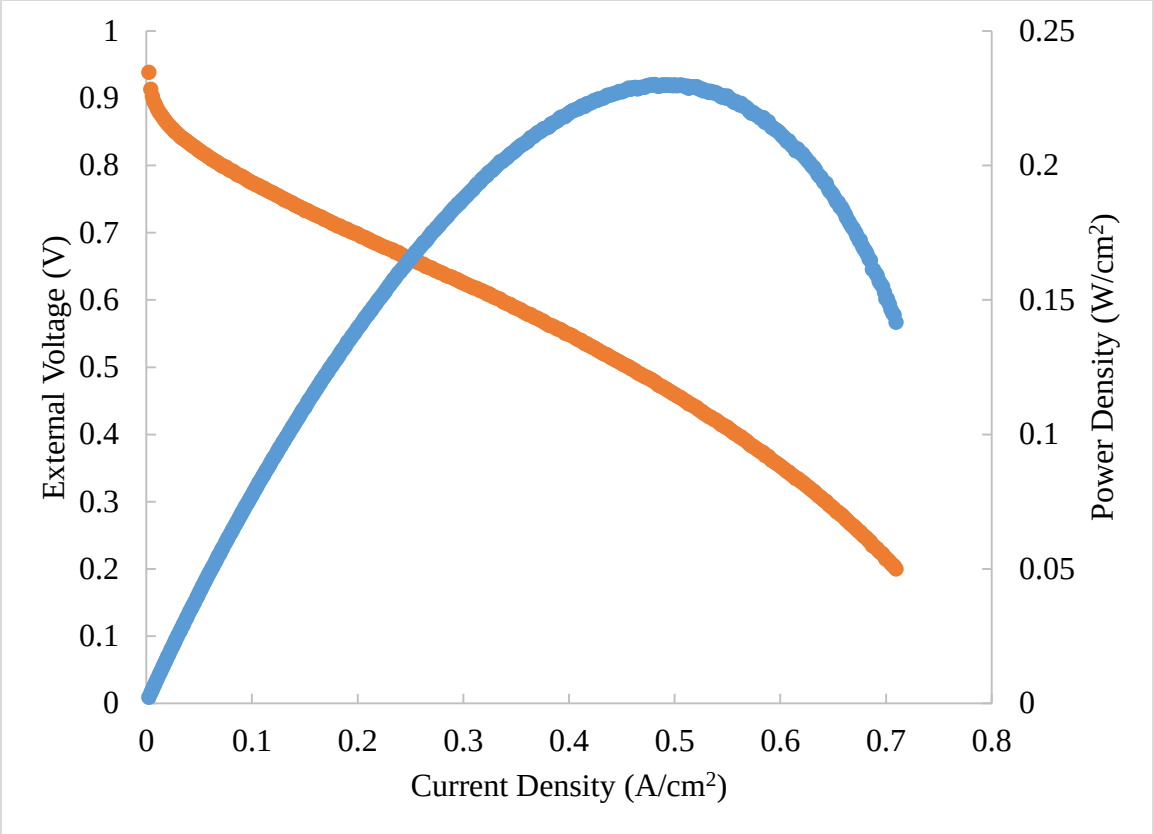

FIGURE 7 – Experimentally Tested Fuel Cell Polarization Curve Using a High Durability MEA

The maximum power density of the high durability MEA was 0.232 W/cm^2 at a cell voltage of 0.485 V and a current density of 0.479 A/cm^2. The peak power output of the fuel cell for a 31.5 cm^2 active area was 7.31 W. As a result of assumptions the peak power output of the simulation was higher than both MEAs experimentally tested; however it is comparable. Simulation, high performance MEA, and high durability MEA had a peak power output of 9.05 W, 8.88 W, and 7.31 W; respectively.

2. Simulation of 100 cm^2 cell without cooling; case 1

The cell simulated in this section has an active area of 100 cm^2 and is shown in Figure 2(a). The cell dimensions are shown in Table 1. The operating cell voltage is set to 0.6 V (SHE). This value was chosen as it is typical for a fuel cell under load. Hydrogen

flow rate is 0.417 L min^{-1} and air flow rate is 2.487 L min^{-1}. Figure 8(a) shows the hydrogen mass fraction in the channels and GDL. The mass fraction is at a maximum of 0.74 at the inlets and decreases to 0.67 at the outlets. Hydrogen mass fraction also decreases as it enters the GDL, which is seen in the enlarged slice. Inlet oxygen mass fraction, Figure 8(b), is 0.23; low oxygen mass fraction is the reason a much higher flow rate is used for air. The mass fraction decreases to 0.15 at the exit. As with hydrogen, the enlarged slice shows mass fraction decrease into the GDL.

Water mass fraction can also be obtained from the data, as shown in Figure 8(c) for the cathode side. Water in the cathode is a result of inlet air humidity and water production via the oxygen and hydrogen reaction. Water mass fraction at the inlet of the cathode channels is 0.023 and increases to 0.11 as flow reaches the exit. The enlarged slice clearly shows higher values of water in the GDL, where the reaction takes place. The pressure gradient shown in Figure 8(d) displays a pressure drop of 3.5 kPa from inlet to outlet, with outlet defined at zero pressure. The enlarged slice shows a clear variation in the pressure of individual channels. Near the outlet, pressure difference in a plane perpendicular to fluid flow may be greater than 200 Pa.

Figure 8(e) shows the temperature variation on the carbon composite material of the bipolar plate. With no cooling, temperature increases from an inlet temperature of 333 K to 348 K at the hottest location near the center. Inlet temperatures are fixed, so the temperatures at the right two corners begin at 333K and quickly increase away from those corners. As fuel flows toward the exit, temperatures increase due to reaction heat, until the temperature reaches a maximum, midway through the last straight section of channels. At the exit, convection heat loss slightly lowers the temperature. Figure 8(f)

displays the outlet velocity profile slice at a position midway between the surface of the plate and the bottom of the channel depth. The Figure 8(f) shows laminar effects with velocity increasing drastically at the outlet. These maximum values may be a result of the simplifications described previously and may thus be inconsequential.

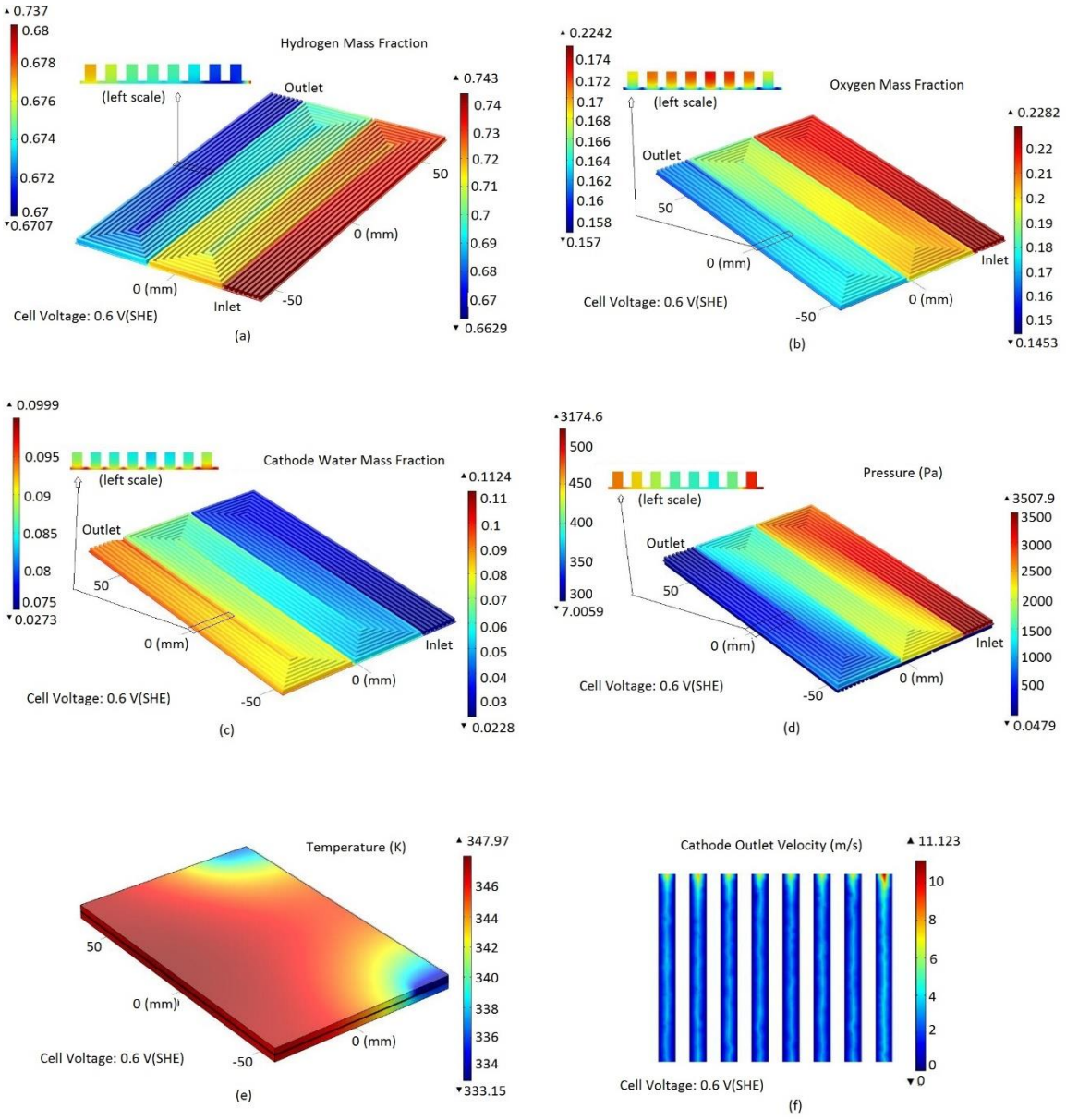

FIGURE 8 - Case 1 without Cooling (a) Hydrogen Mass Fraction Profile, (b) Oxygen Mass Fraction Profile, (c) Water Mass Fraction in the Cathode Channels, (d) Pressure Drop in the Cathode Channels, (e) Temperature Profile of the Cathode Side Bipolar Plate, and (f) Outlet Velocity Gradient Close-Up of Air Flow (Cell Voltage: 0.6 V)

3. Simulation of 100 cm^2 cell with water cooling; case 1

This section aims to simulate the same fuel cell as section 2; however, water cooling is now involved. It appears from the simulation data that a fuel cell may be able to operate without cooling. That may be true with a single cell; however, to get a usable power output, cells are generally stacked in series. The cells in the middle of the stack will not receive the same benefit of convection to the flowing gas that a single cell does. Gas entering the next cell from an endplate will be at a higher temperature, so the effect compounds as it continues to the middle of the stack. This calls for a cooling system implementation. For case 1, cooling channels are implemented in between anode and cathode interfaces that do not contain an MEA. Water enters the channels at a set temperature of 333 K.

Flow rates are identical to those in the previous simulation of case 1. The flow rate of water, an easily adjusted value, is set equal to the flow rate of air for the current simulation. Operating cell voltage is 0.6 V. Figure 9(a) shows the hydrogen mass fraction entering the cell at the same mass fraction as the previous simulation, 0.74. The exiting mass faction is, however, slightly higher, with a value of 0.69. The reason for this will be discussed shortly. The enlarged slice displays decreased hydrogen mass fraction into the GDL. Oxygen mass fraction, shown in Figure 9(b), enters at 0.23 as before. The oxygen mass fraction at the exit is lower than in the previous simulation, at 0.18. Cathode water mass fraction, seen in Figure 9(c), enters at 0.023 and exits at 0.074. The inlet value of water mass fraction is the same as before, while the outlet has decreased.

Figure 9(d) displays the pressure distribution in the cathode channels. Pressure at the inlet is 3.99 kPa and the outlet is set to zero pressure. The inlet pressure value is greater

than in the previous simulation. Variation in fluid viscosity is a possible explanation. Figure 9(f) shows a maximum outlet velocity of 9.47 m s^{-1}. The velocity reaches its maximum right at the outlet boundary. A slight variation in velocity between channels is seen; possibly a result of channel geometry. Channels which change direction more drastically have more variation in velocity.

The temperature profile on the carbon composite bipolar cathode plate, along with the water channel volume, is shown in Figure 9(e). Water cooling of the cell is effective, as the highest temperature has decreased to 335 K from 348 K. This observation explains what was found above; for the simulation with cooling compared to that without, hydrogen and oxygen mass fraction is higher at the outlet while water mass fraction is lower. There is obviously not as much reaction occurring for the simulation with water cooling. The decrease in temperature has also decreased the activation potential of the hydrogen and oxygen. This may seem like a hindrance at first, but when considering a full stack of, say, 16 cells, temperatures will be higher and cooling important. Stack temperature can be controlled by water cooling flow rate.

These results are quite promising. The simulations produce logically valid scenarios and values. They are lacking, however, without experimental verification. Even so, the values are in agreement with typical values seen in referenced documents.

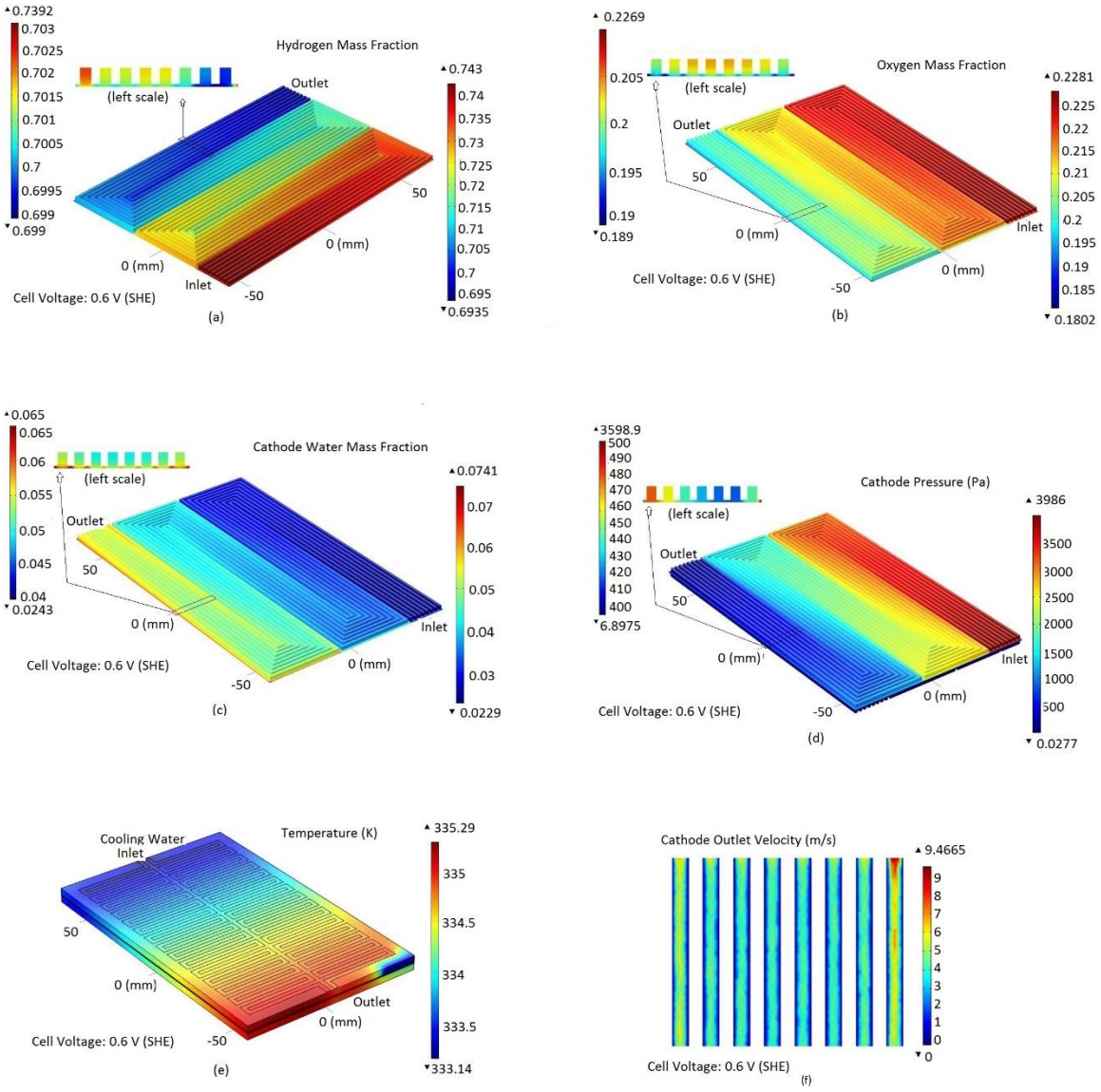

FIGURE 9 - Case 1 *with* Cooling (a) Hydrogen Mass Fraction Profile, (b) Oxygen Mass Fraction Profile, (c) Water Mass Fraction in the Cathode Channels, (d) Pressure Drop in the Cathode Channels, (e) Temperature Profile of the Cathode Side Bipolar Plate, and (f) Outlet Velocity Gradient Close-Up of Air Flow (Cell Voltage: 0.6 V)

4. Simulation of 200 cm^2 square cell with air cooling; case 2

In this section and the next, simulation results of a unique fuel cell design are presented. The goal of this design is to improve thermal distribution and thermal management control and to implement air cooling as opposed to water cooling. Air cooling will reduce weight and potential for leakage that may disrupt fuel cell

performance. Also, with an air cooled stack, there is a possibility of using the same air for cooling that is supplied to the cathode. This will make the stack more compact, thus further reducing weight. This design could also provide better clamping pressure distribution; however, that will not be explored in this thesis. The flow rate used here, 0.834 L min^{-1} for hydrogen and 4.974 L min^{-1} for oxygen, is two times that used in case 1. Other than flow rate, all parameters are identical to case 1. Cell operating voltage is set to 0.6 V.

The hydrogen mass fraction is shown in Figure 10(a) with a maximum value at the inlets of 0.74 and outlets at 0.72. The lowest value of mass fraction is found in the GDL. The enlarged slice shows the decrease in hydrogen mass fraction as it travels to the GDL. The outlet value is slightly higher than that for case 1. This may be attributed to a larger flow rate and active area. The variation of mass fraction in a set of channels is insignificant. Figure 10(b) displays the oxygen mass fraction. Inlet mass fraction is 0.2286, while mass fraction at the outlet is 0.21. The GDL, as with oxygen mass fraction, has the lowest mass fraction of oxygen, nearing zero in some areas.

Figure 10(c) shows the water concentration in the cathode side of the cell. The inlet water mass fraction is 0.0224, and the outlet is 0.04. The highest values of mass fraction, 0.2639, are found in the GDL where the reaction occurs. That means that the majority of the water produced in the cell is stagnating in the GDL. This will drastically reduce performance and efficiency. However, this result may also be explained by simulation error. The GDL is much larger than the active area of the fuel cell, which might contribute to simulation error. The enlarged slice shows the mass fraction of water increase into the GDL; this is expected.

The pressure in the cathode side of the cell is shown in Figure 10(d). Pressures correspond well with case 1. The maximum pressure at the inlets is 2.38 kPa, while the outlet is set to zero. Pressure is very evenly distributed and has little variation between channel sets, as seen in the enlarged slice. Outlet velocity profile is shown in Figure 4(f). Laminar flow is apparent, and the highest velocity is 11.8 ms^{-1}. Velocity distribution is relatively even with differences due to individual channel geometry.

Temperature gradients of the cathode cooling air volumes and bipolar plate are shown in Figure 10(e). The highest temperature, 339 K, is about 4K above that of case 1 with cooling. This is a great result, as the case 2 fuel cell only uses forced air convection for cooling. The distribution of temperature is also very nice. Two sides of the outer edges contain the hot spots. These hot spots are pulled away from the center of the cell, which will allow better thermal management control. It may be possible to increase the convection occurring at the edges, in a simple and cost-effective way. This allows almost full control of temperature distribution within the cell.

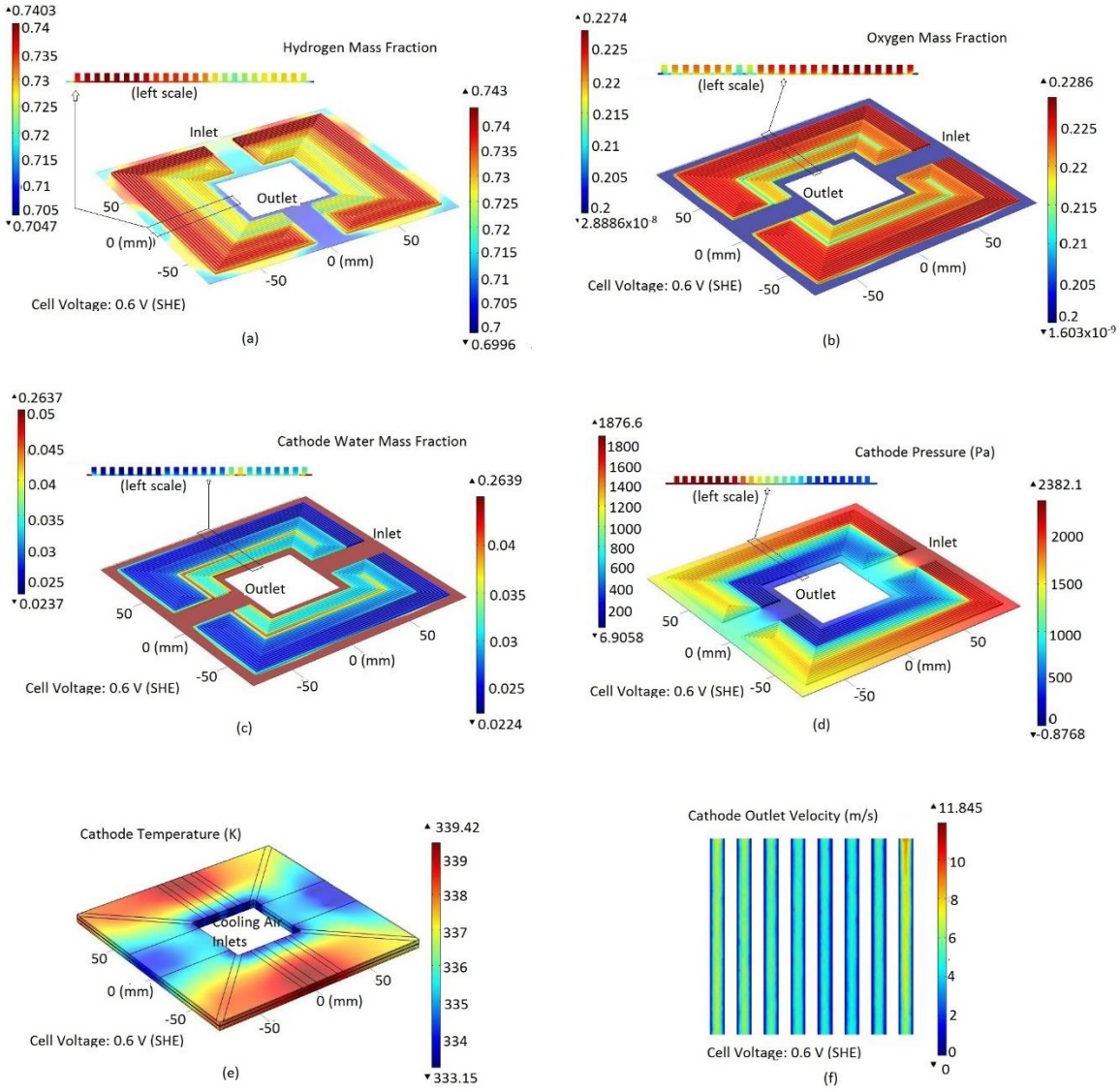

FIGURE 10 - Case 2 with Forced Air Cooling (a) Hydrogen Mass Fraction Profile, (b) Oxygen Mass Fraction Profile, (c) Water Mass Fraction in the Cathode Channels, (d) Pressure Drop in the Cathode Channels, (e) Temperature Profile of the Cathode Side Bipolar Plate, (f) Outlet Velocity Gradient Close-Up of Air Flow (Cell Voltage: 0.6 V)

5. Simulation of 200 cm^2 alternative square design with air cooling; case 3

The major difference between this design and that of section 4 is the gas channel pattern and overall cell shape. The center hole is much larger than before. The cell sides, from outer edge to inner edge, are thinner in comparison, which, it is hoped, will increase thermal management control and decrease the air flow rate needed for cooling. This

simulation uses the same flow rates as case 2. In fact, all parameters are identical, save for the design of the cell itself.

Figure 11(a) shows the hydrogen mass fraction at an inlet value of 0.74, with a minimum of 0.70 in the GDL. The enlarged slice shows a variation in hydrogen mass fraction of the channels; however, when considering the scale, it is minute. The minimum value of 0.70 is off-putting at first glance, but it makes sense in conjunction with the increased flow rate. More oxygen is entering the cell per unit time, so the value at the outlet need not be reduced as much for sufficient power output. Figure 11(b) displays the oxygen mass fraction with a maximum of 0.23 and a minimum value at the outlets of 0.20. This minimum is only slightly higher than that of case 1 with cooling. This can be explained by the same reasoning as used for the hydrogen: increased flow rate. Both hydrogen and oxygen have minimums in the GDL. It may be prudent in the future to reduce the size of the GDL to more closely fit the active area.

Cathode water mass fraction is shown in Figure 11(c). The scale in the Figure has been significantly adjusted, to display the variation within the channels. The highest water mass fraction, 0.26, occurs in the GDL, as it should. The mass fraction in the channels only reaches a maximum of 0.06. A possible explanation is that the number of bends in the design hinders water flow in such a way that it stagnates in the GDL. This would significantly reduce performance in a real fuel cell. Figure 11(d) is the pressure variation in the cathode side of the cell. The maximum pressure, 11.4 kPa, occurs at the inlet, while the outlets are defined as zero pressure. Outlet velocity, shown in Figure 11(f), displays a maximum velocity of 13.7 m s^{-1}. This value is higher than in both

simulations of case 1. This means that the drastic increase in pressure is due only to increased flow rate.

Figure 11(e) shows the temperature distribution in the cathode side of the fuel cell. The larger surface areas are those of cooling air volume. Thin strips are from the carbon composite bipolar plate. Reducing the contact area of the bipolar plate this drastically may lower the performance of the cell. This consequence is not tested in the current simulation. The maximum temperature occurring in this cell is 335 K, which compares to case 1 with water cooling. This shows that air cooling has real potential in being sufficient for stack cooling. The distribution is also promising in that hot spots occur at the outside corners. Pulling the hotspots away from the center of the cell allows for easier control. This simulation supplies a boundary for convection to the outside air at the edges of the carbon composite bipolar plate. Because of the position of the hot spots, this convection to outside air may be increased, using methods to increase surface area at the edges such as implementing small fins along the edge surface. Table V shows the resulting highest temperature and temperature change for the simulations presented above.

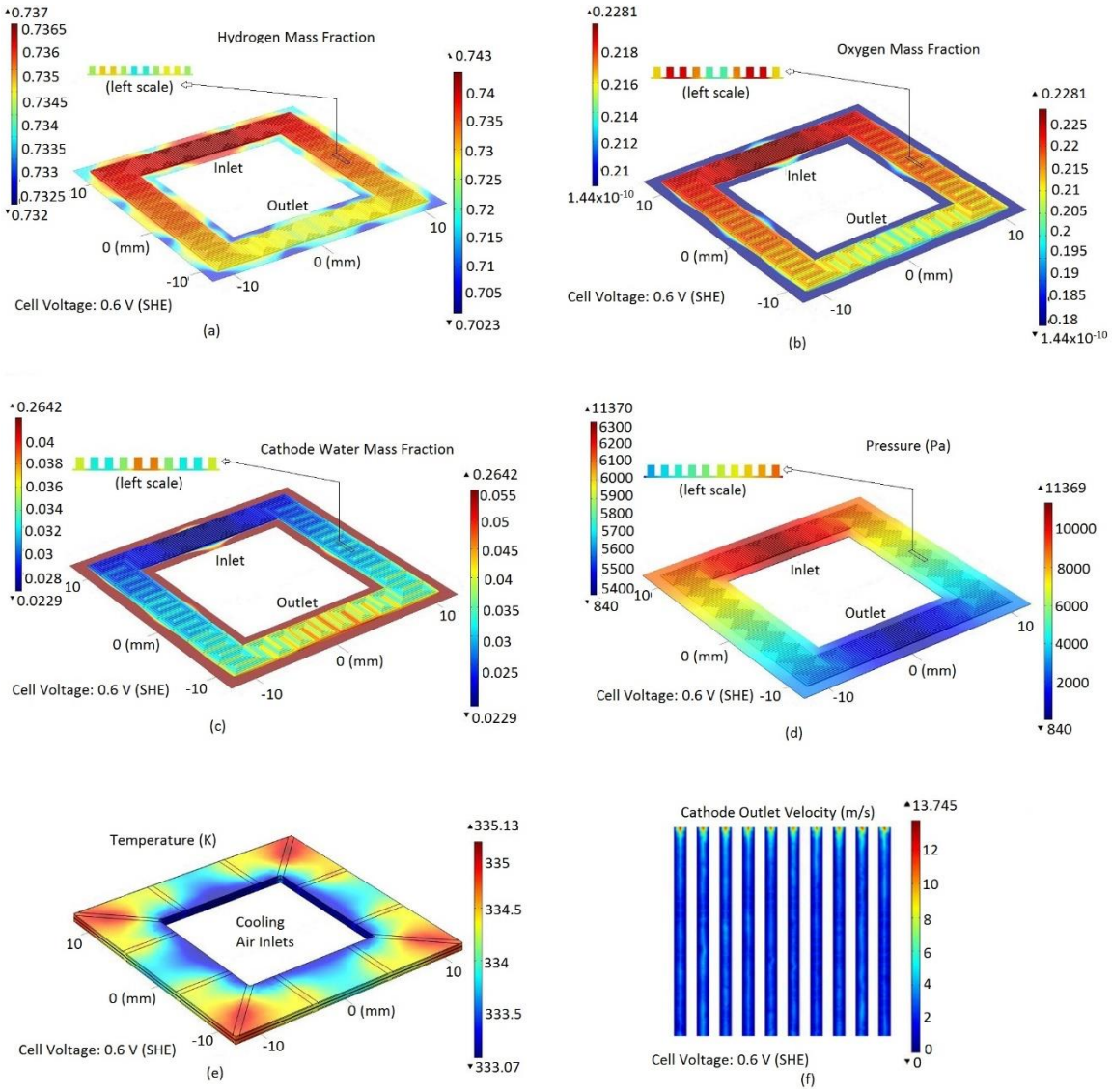

FIGURE 11 - Case 3 with Forced Air Cooling (a) Hydrogen Mass Fraction Profile, (b) Oxygen Mass Fraction Profile, (c) Water Mass Fraction in the Cathode Channels, (d) Pressure Drop in the Cathode Channels, (e) Temperature Profile of the Cathode Side Bipolar Plate, and (f) Outlet Velocity Gradient Close-Up of Air Flow (Cell Voltage: 0.6 V)

TABLE V

TEMPERATURE VARIATIONS

Design	Case 1, no cooling	Case 1, water cooling	Case 2, air cooling	Case 3, air cooling
Highest Temperature [K]	347.97	335.29	339.42	335.13
Inlet gas [K] (cooling and fuel)	333	333	333	333
Temperature change [K] (ΔT)	14.97	2.29	6.42	2.13

B. Compression

A new square fuel cell design will improve efficiency, through better thermal management, and reduce weight of the fuel cell system. Square cross sections have been hypothesized to improve the performance of fuel cells because every active area is adjacent to an area equal and constant in width, helping to increase output (Heinzel, Nolte et al. 1998). Reduced weight of the BoP is a result of a reduced need for cooling management and a reduction in demand for oxygen delivery and water removal. Since the novel design has a more direct and open path for air/oxygen then the traditional fuel cell, less expensive devices can be implemented for the air/oxygen delivery systems; this includes considerations of water removal.

Using 200 cm^2 active area cells reduces contact resistance by decreasing the number of cells required to reach a desired power output. The stack also offers a better compression mechanism in that bolts are placed inside the center hole as well as around the outside of the stack. This has the potential to decrease leakage, decrease fuel crossover, and increase efficiency.

1. Single Cell with 5000 N Axial Load

A 5000N axial load was applied to the bolt locations of a single cell stack. Figure 12(a) displays the stress plot for an end-plate with a maximum stress of 105.3 MPa

occurring near the bolt holes. Stress is on average much lower, around 40 MPa, reducing toward zero in the center. Shown in Figure 12(b) is the stress plot across a bi-polar plate. The maximum stress is 33.7 MPa occurring near the channel inlet and outlet. The average stress across the bi-polar plate is much lower than the end-plate at about 15 MPa. Very low stress occurs inside the channels, which is expected because it is not in direct contact with another material.

Figure 12(c) shows the stress plot of the GDL. The maximum stress is 3.9 MPa and occurs where the bi-polar plate contacts the GDL. This image shows an exaggerated deformation with a scale factor of 5. The gold rectangle represents the non-deformed shape. The idea is that stress lines will occur on the GDL due to channels in the bi-polar plate (Lee 12005). Figure 12(d) shows the stress plot of the MEA. The maximum stress in this layer is 13.7 MPa and occurs at the corners. This image shows a true scale deformation. It is seen that the MEA is much more susceptible to deformation. The reduced stress area in the center comes from the reduced stress in the GDL. The gasket surrounding the GDL is taking the majority of the clamping pressure here.

These results are very telling of the stack configuration. It is obvious that uniform stack compression throughout the face of the GDL is impossible. The center of every layer will inevitably have reduced clamping pressure. This can be problematic for several reasons and must be addressed.

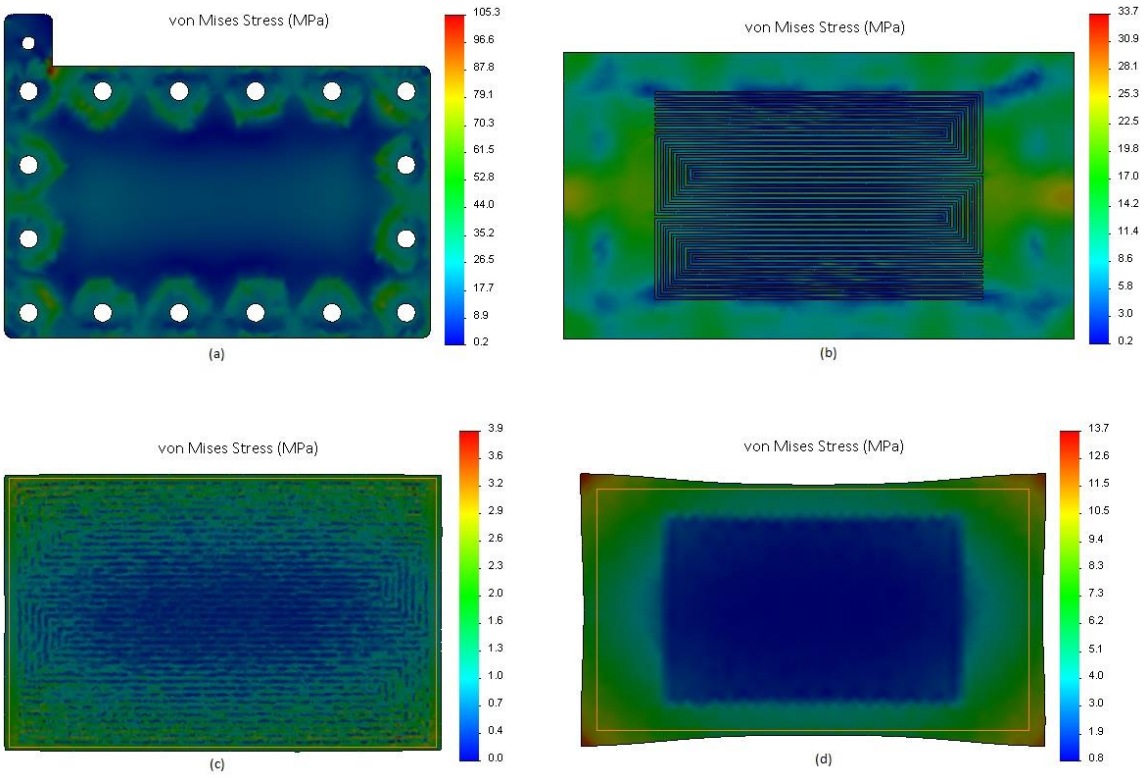

FIGURE 12 – 5000 N Axial Load (Single Cell, Active Area=100 Cm^2): (a) End-Plate Stress Plot, (b) Bi-Polar Plate Stress Plot, (c) Deformed GDL Stress Plot, and (d) Deformed MEA Stress Plot

2. Single Cell with 5.65 N·m (50 in·lb) Torque

The goal with this simulation is to add more realism. When assembling the stack, the bolts will experience torque which is easily measured. Torque is converted to axial load in a nut and bolt assembly by thread contact. Analytically, a simplified conversion is performed using

$$P = f * W * D \tag{22}$$

where P is the axial load, *f* the friction factor, W the torque, and D is the bolt diameter. The simulation performed here takes more factors into account. This means thread pitch,

bolt diameter, and friction factors must be taken into consideration during assembly. A friction factor of 0.2 is assigned here with a torque of 5.65 N·m. Aside from applying a torque as opposed to an axial load; the model is identical to the model described above.

Figure 13(a) shows the stress plot on an end-plate with a maximum stress of 79.9 MPa and an average stress of roughly 25 MPa. The values are lower than before but the stress distribution is quite similar. A 5.65 N·m torque is somewhere in the vicinity of a 1000 N axial load. The next stress plot in Figure 13(b) is of the bi-polar plate. A maximum stress of 19.9 MPa occurs at the inlets and outlets of the channels with an average stress around 10 MPa.

The stress plot across the GDL is shown in Figure 13(c) with a deformation scale factor of 10. The gold rectangle shows the original shape. A maximum stress of 2.4 MPa is found and an average stress of about 1.0 MPa. The concern presented in the bi-polar plate is made plainly evident from this image. The stress over the center, at least 30% of the whole area, is very nearly zero. Electrons will be hard pressed to travel through this area. Figure 13(d) gives a reason for this, showing the stress in the MEA. A maximum stress of 9.5 MPa occurs at the corners and an average of about 3 MPa throughout. A deformation scale factor of 5 is shown here. In order to seal the stack gaskets are used, this material takes the stress that would otherwise go through the GDL. Because of this the center of the MEA, the area contacting the GDL, is almost zero.

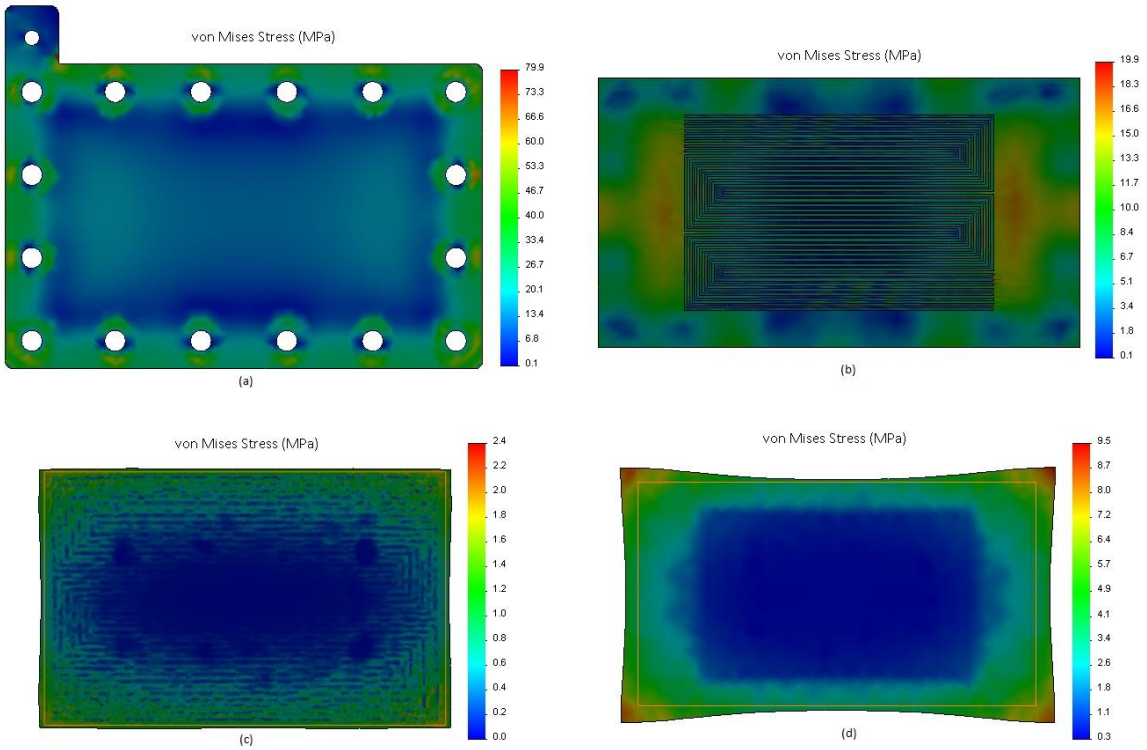

FIGURE 13 - 5.65 N·m Torque (Single Cell, Active Area=100 Cm^2): (a) End-Plate Stress Plot, (b) Bi-Polar Plate Stress Plot, (c) Deformed GDL Stress Plot, and (d) Deformed MEA Stress Plot

3. Single Cell with 10.17 N·m (90 in·lb) Torque

The stress across the interface between the bi-polar plate and the GDL is too low with 5.65 N·m of torque so it is increased here to 10.17 N·m. The objective is to get closer to a goal of 1 MPa clamping pressure across the majority of the GDL (Lee, Hsu et al. 2005). The maximum stress increased to 143.8 MPa in the endplate, shown in Figure 14(a). The stress distribution remains the same, however; an increase is seen in the central area. Stress on the bi-polar plate has increased to a maximum of 36.9 MPa shown in Figure 14(b).

The average stress across the GDL, Figure 14(c), has increased to about 2 MPa. The center is still very close to zero. This suggests a change in stack assembly or bolt configuration should be encouraged. Contact resistance will be very high in the center

which can substantially reduce performance. Increasing assembly torque beyond this point has the potential to start destroying materials. Figure 14(d) shows the stress plot on the MEA with a true scale deformation that is substantial.

These images present two detrimental aspects of this stack design. The bolt configuration results in near zero stress at the interface between GDL and bi-polar plate. This is highly undesirable as it results in high contact resistance. The other factor acting to exaggerate this issue is the silicon gasket. It is not allowing enough compression in the GDL for proper contact. More torque could solve this problem, however; the gasket carries the force through to the MEA causing it to deform in a way that could rupture the material. A better solution might be adjusting the thickness of the gasket.

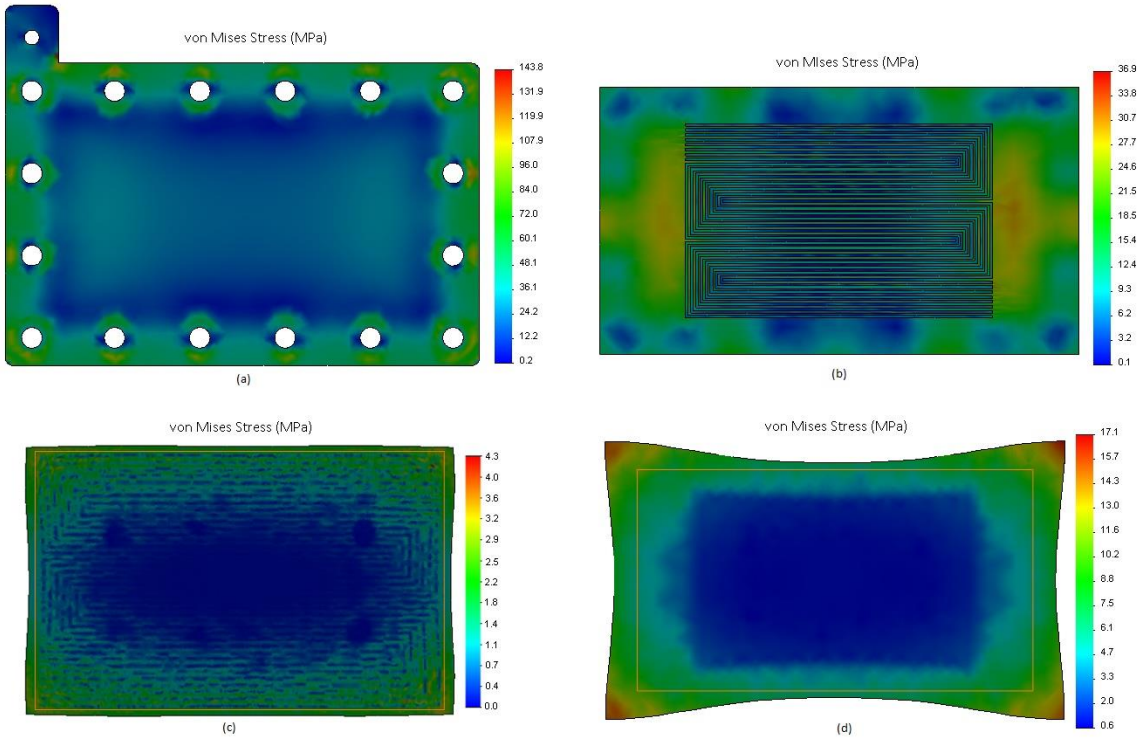

FIGURE 14 - 10.17 N·m Torque (Single Cell, Active Area=100 Cm^2): (a) End-Plate Stress Plot, (b) Bi-Polar Plate Stress Plot, (c) Deformed GDL Stress Plot, and (d) Deformed MEA Stress Plot

4. Fuel cell stack, 16 cells, 5000 N per bolt, all layers

The model discussed in this section has 16 cells and includes all the layers of the single cell model; GDLs, MEAs, bi-polar plates, and gaskets. A 5000 N axial load is applied to each bolt.

A stress plot on an exploded view of the stack is shown in Figure 15(a). It is seen from this Figure that the end plates, of course, take the brunt of the stress due to clamping force. Figure 15(b) shows the true scale, resultant replacement deformation on an exploded view of the stack. This makes evident that something needs to be adjusted in the configuration because the MEAs have a displacement of over 8 mm in some area. All other layers have relatively small displacements. Figure 16(a) is of an endplate. The

highest regions of stress occur around the bolt holes up to 195 MPa. Low regions of stress arise at the center while near the corners of the plate, stress is almost zero.

The stress plot across the first bipolar plate in the stack is shown in Figure 15(c). The highest stress occurs along the left and right edge at a value of 17.8 MPa. There are regions of low stress near the corners. This is possibly due to the bolt configuration and/or way in which the endplates are flexing. The regions of low stress also seem to correspond with regions of low stress on the end plates. Displayed in Figure 15(d) is the stress plot on the first MEA in the stack at a scale factor of two. The gold rectangle represents the original shape of the MEA. All four corners receive the maximum stress of up to 7.2 MPa. The left and right edges appear to be the most deformed while the center incurs relatively low stress.

Figure 15(e) shows the stress plot on the first GDL in the stack with a scale factor of 20. The stress here is much more uniform however it is only has a maximum stress of 1.5 MPa. Most of the GDL is near 1 MPa. This can cause high contact resistance in the stack and drastically lower performance. The gasket that surrounds the GDL is shown in Figure 9(f) at a scale factor of 20. The gasket has a much higher stress range than the GDL with a maximum at 41.9 MPa. This means the gasket may be too thick or too rigid for the GDL thickness used. The gasket is absorbing all the force of the clamping pressure and very little is transferred to the GDL. It can also be seen that the gasket push out in the middle causing high stress on the inside corners.

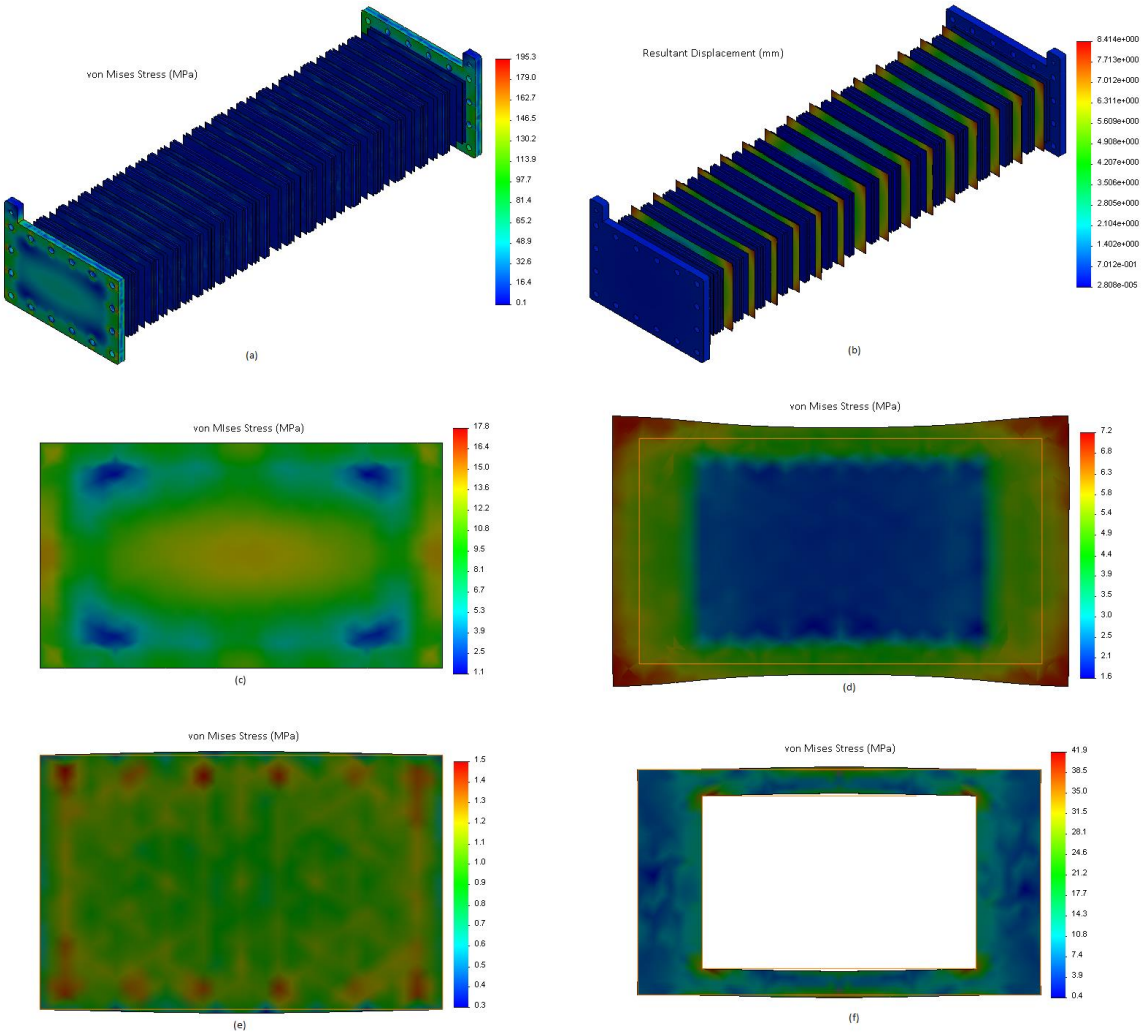

FIGURE 15 - 5000N Axial Load (16 Cell Stack: 100 Cm^2 Active Area/Cell): (a) Exploded 16 Cell Stack Stress Plot, (b) Exploded 16 Cell Stack Displacement Plot, (c) First Cell Bipolar Plate Stress Plot, (d) First Cell MEA Stress Plot, (e) First Cell GDL Stress Plot, and (f) First Cell Gasket Stress Plot

In order to examine the effects of clamping pressure throughout a 16 cell stack, images are presented of layers in the eighth cell; the middle of the stack. Figure 16(b) is of the bipolar plate. The maximum stress has decreased by about 4 MPa but, more importantly, the stress plot has changed shape. Now very low areas of stress dominate the center of the plate. The left and right edges still contain the highest stress values. The MEA is shown in Figure 16(c) with a scale factor of 2. There appears to be no significant

change between the first MEA and eighth MEA stress plot. The image shown in Figure 16(d) is of an MEA taken out of the stack used for experimental work. The MEA was warped, so it was placed under an acrylic endplate in order to keep it flat. This MEA has a Teflon outer band for structure. The MEA was subjected to the heat and clamping pressure of an operating stack and has warped in a manner consistent with the simulations.

The GDL of the eighth cell is shown in Figure 16(e) with a scale factor of 20. It seems that the stress is nearly the same here however; this GDL seems have a higher concentration of high stress areas. The mesh appears to be protruding through these results, this may be the cause. Figure 16(f) shows the gasket surrounding this GDL at a scale factor of 20. The stress here increased substantially, by 5 MPa. Although the stress plots are very similar, a logical explanation for the increase in stress is not evident outside of simulation error.

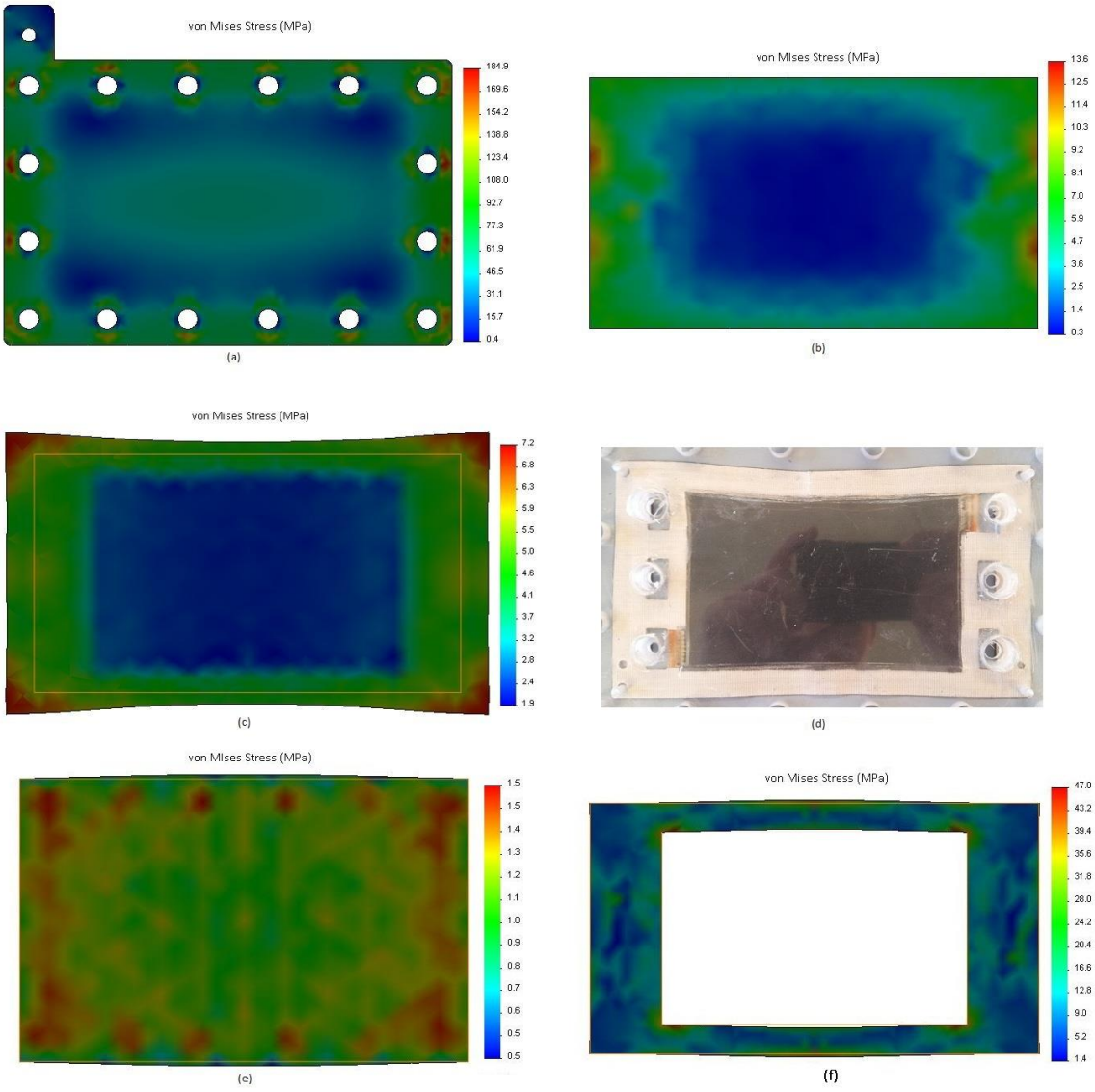

FIGURE 16 – 5000 N Axial Load (16 Cell Stack: 100 cm^2 Active Area/Cell): (a) End Plate Stress Plot, (b) Eighth Cell Bipolar Plate Stress Plot, (c) Eighth Cell MEA Stress Plot, (d) Eighth Cell MEA Deformation From Experimental Work, (e) Eighth Cell GDL Stress Plot, and (f) Eighth Cell Gasket Stress Plot

5. Fuel cell stack, 16 cells, 10.17 N·m per bolt, all layers

The next model was simulated in order to increase realism by switching from an axial load to a torque load. It is identical to the model in section 4 except the bolt load is now 10.17 N·m Figure 17(a) is an exploded view of the stack showing stress plots on all the materials. The endplates are, again, taking most of the stress with a maximum of

193.3 MPa, only slightly lower than the 5000 N axial load case. Distributions appear similar as they should. Figure 17(b) is the exploded view resultant displacement plot. The maximum deformation in the MEA layer is over 8 mm. The model needs adjustment. Figure 18(a) displays the stress plot on the end plate of that 16 cell stack. The maximum stress occurs near the bolt holes at a value of 183.1 MPa, only slightly lower than the section 4 case.

Figure 17(c) is of the first bipolar plate's stress plot with a maximum stress of 17.6 MPa. Stress distributions in the bipolar plate are a bit odd with near zero stress a short distance from the corners.

Stress in the center of the plate is quite high. This could be just a matter of the plate being so close to the area of clamping pressure application. Figure 17(d) shows the stress plot on the first MEA with a deformation scale factor of 2 and the original shape a gold rectangle. High stress up to 7.1 MPa occurs at the corners while stress drops toward zero in the center to 1.6 MPa. The stress around the sides of the MEA is causing large deformations.

The first GDL of the stack is shown in Figure 17(e). The highest stress occurs near the sides at a value of 1.5 MPa. Stress drops to around 1.0 MPa in the center of the GDL. Figure 17(f) displays the gasket that surrounds the GDL. A maximum stress of 41.5 MPa occurs at the inside corners of the gasket while most other areas have less than 10 MPa of stress. The gasket is taking most of the pressure applied to this layer of the stack. This means the GDL is being deprived of stress needed to lower contact resistance.

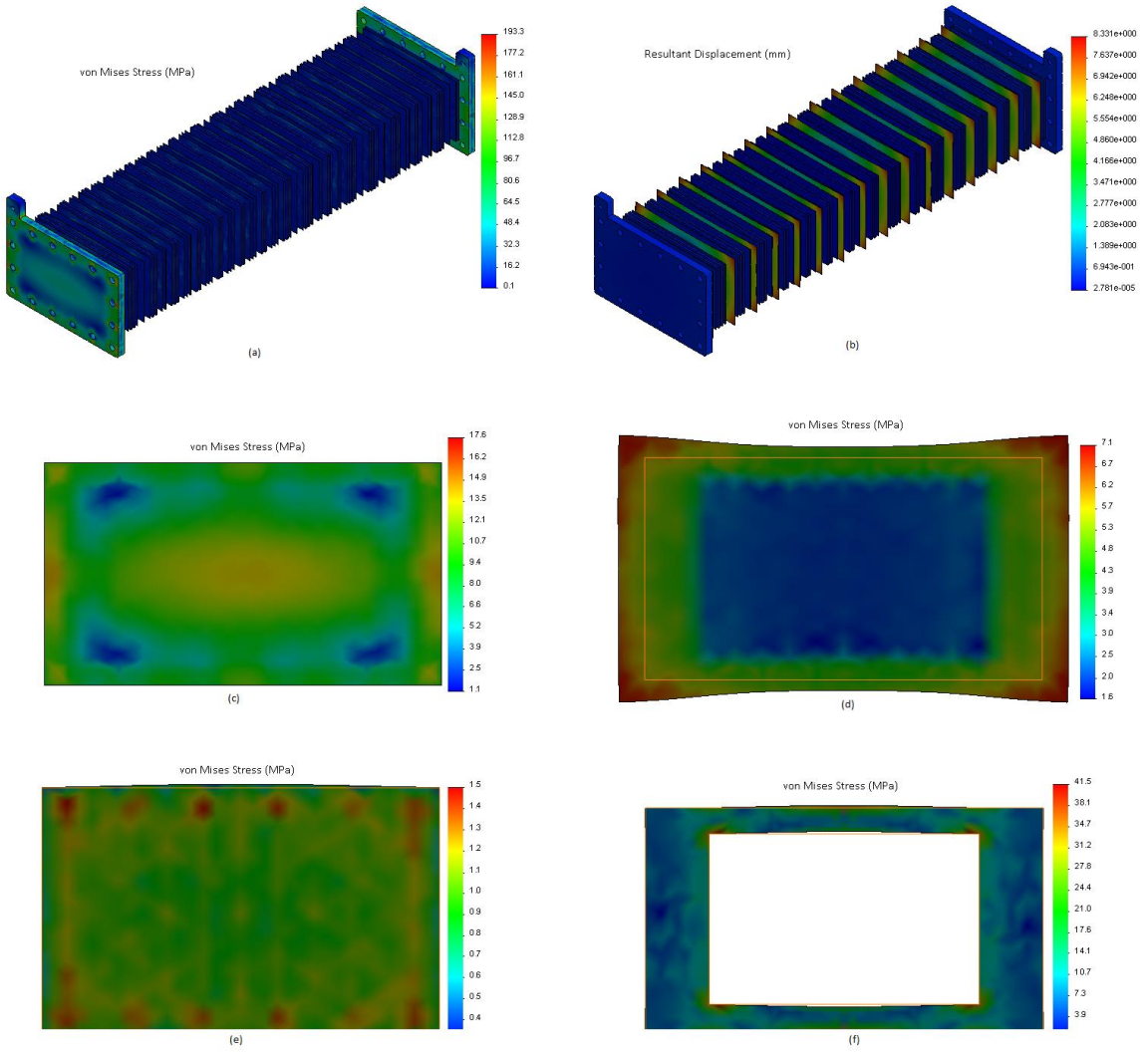

FIGURE 17 - 10.17 N·m Torque (16 Cell Stack: 100 cm^2 Active Area/Cell): (a) Exploded 16 Cell Stack Stress Plot, (b) Exploded 16 Cell Stack Displacement Plot, (c) First Cell Bipolar Plate Stress Plot, (d) First Cell MEA Stress Plot, (e) First Cell GDL Stress Plot, and (f) First Cell Gasket Stress Plot

Stress plots of layers near the middle of the 16 cell stack, the eighth cell from an endplate, will be shown next. This is done to display the variation of clamping pressure throughout a multi cell stack. Figure 18(b) shows the stress plot on the eighth cell's bipolar plate. The maximum stress occurs at the edges and is 13.5 MPa. The stress distribution shown here is expected. The sides contain most of the stress while the center is near zero. The other layers shown are nearly identical to those of the first cell in

distribution, range, and magnitude. Figure 18(c) is the MEA of the eighth cell, Figure 18(e) the GDL and, Figure 18(f) the gasket. A small increase in stress is seen in the GDL and gasket layers which may be a result of the mesh being too large. An image of a warped MEA taken from an experimental 16-cell stack is shown in Figure 18(d). The warping is consistent with that shown in simulation.

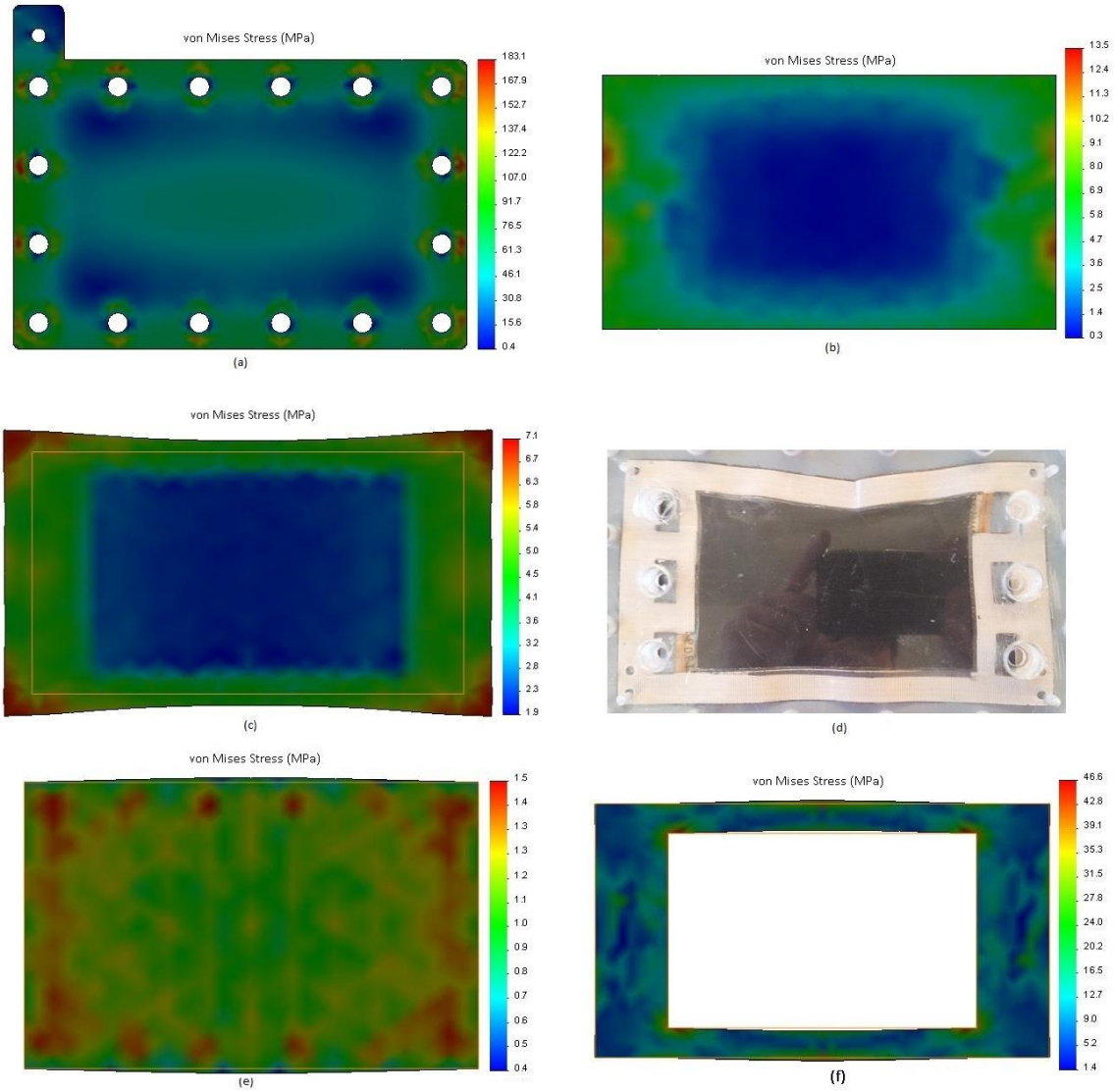

FIGURE 18 - 10.17 N·m Torque (16 Cell Stack: 100 cm^2 Active Area/Cell): (a) End Plate Stress Plot, (b) Eighth Cell Bipolar Plate Stress Plot, (c) Eighth Cell MEA Stress Plot, (d) Eighth Cell MEA Deformation From Experimental Work, (e) Eighth Cell GDL Stress Plot, and (f) Eighth Cell Gasket Stress Plot

A summary of the maximum stress in each layer for all cases is shown in Table VI. The 16 cell stack appears to have an acceptable loading on most materials; however, the gasket stress is too high. In reality, this may cause stress concentrations high enough to form crack in the brittle bipolar plate.

TABLE VI

MAX STRESS IN MPA FOR EACH MATERIAL

Study	**Single Cell 5000 N Axial Load**	**Single Cell 5.65 N·m Bolt Torque**	**Single Cell 10.17 N·m Bolt Torque**	**16 Cell Stack 5000 N Axial Load**	**16 Cell Stack 10.17 N·m Bolt Torque**
End plate	105.3	79.9	143.8	184.9	183.1
Bipolar	33.7	19.9	36.9	17.8	17.6
MEA	13.7	9.5	17.1	7.2	7.1
GDL	3.9	2.4	4.3	1.5	1.5
Gasket	23.2	9.5	17.1	41.9	41.5
8^{th} cell results below					
Bipolar				13.6	13.5
MEA				7.2	7.1
GDL				1.5	1.5
Gasket				47.0	46.6

The series of simulations shown in this thesis exemplifies the importance of considering clamping pressure when building a FC stack. Studying clamping pressure on a single cell is not necessarily enough. Adding cells drastically changes stress applied to each individual cell. If the center cell/s has a high contact resistance, the performance of the whole stack is reduced. A compromise must be made when finding the optimum clamping pressure. It might be prudent to simulate a stack by increasing the number of cells one at a time. This way you can examine each step and decide if that number of cells is asking too much of your assembly. For example, it may be better to run two 10-cell stacks as opposed to one 20-cell stack.

6. Experimental Load Testing

The effects of load on GDL thickness were tested for applied load of 0.5 to 2.5 MPa in increments of 0.5 MPa. Results are shown in Figure 19. The starting thickness of a coated GDL is 0.22 mm. It is seen that there is a gradual reduction in thickness from 0.22 mm to 0.177 mm. The non-coated GDL begins at 0.14 mm and decreases to 0.08 mm at 2.5 MPa. The tendency of reduction in thickness with the application of load gradually decreases. After a point, there will be very little effect of the applied load on the thickness of the GDL.

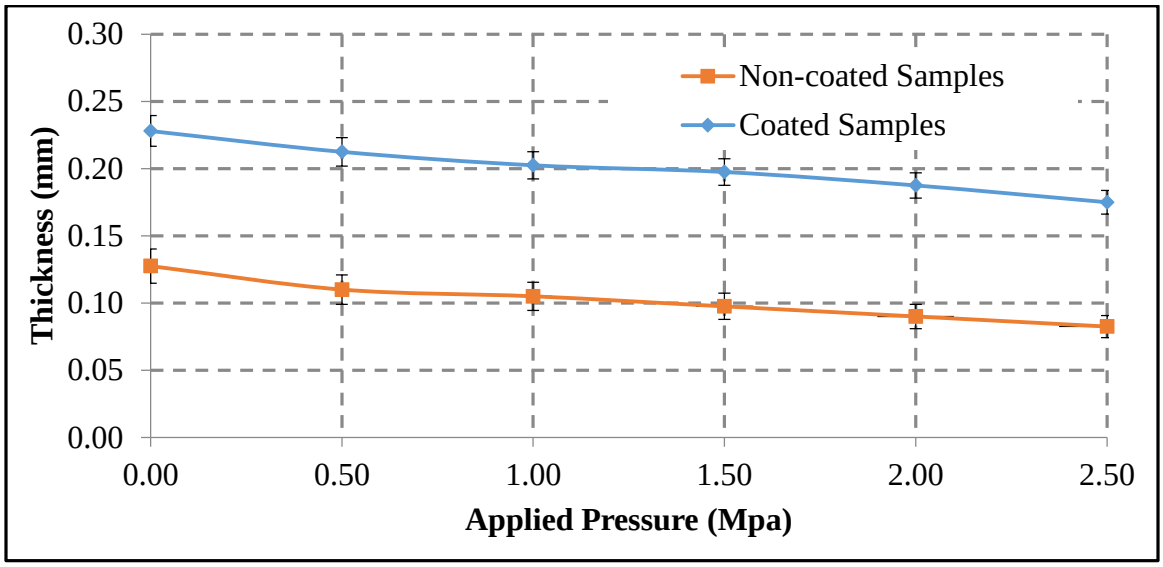

FIGURE 19 - Effects of Compressive Loading From 0.5 MPa To 2.5 MPa in Increments Of 0.5 MPa for 10 Minutes Each. The Data Points on the Top Represent the Coated GDL and the Data Points at the Bottom Represent the Non-Coated GDL. The Vertical Error Bars Represent the Percentage Error In Measurement to an Approximation of 5%

Results from clamping pressure method one of cells 1, 3, 5, and 7 is shown in Figure 20(a-d). The pressure sensitive films in Figure 20 show very little color which means pressure on the GDL is severely lacking throughout the stack. The magnitude of pressure on the GDL appears to increase closer to the center of the stack. As seen in the simulations, pressure is highest at the edges and near zero at the center of a GDL.

Clamping pressure method two results from cells 1, 3, 5, and 7 are shown in Figure 21(a-d). A much deeper coloration is seen in these images indicating that the GDL is under increased pressure compared to method one. Between method one and two, the torque and load applied via hydraulic press are identical. The difference is a static weight used in method two. This indicates that duration may be a cause or solution to clamping pressure concerns.

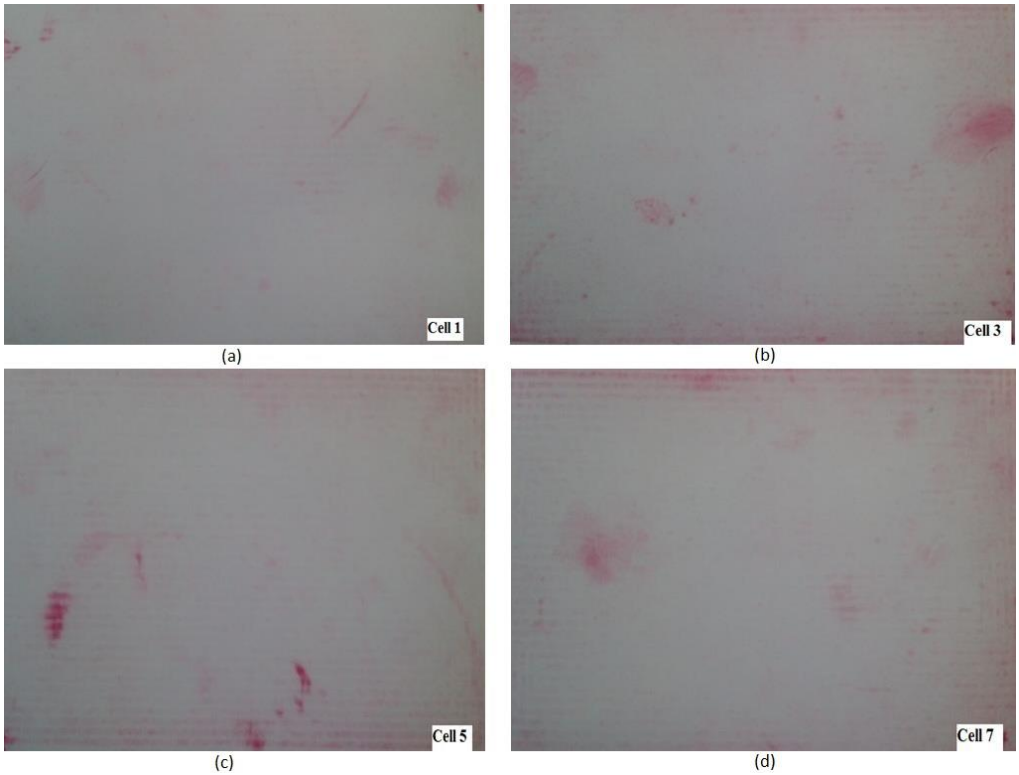

FIGURE 20 - Pressure Sensitive Film in a 16-Cell Stack Using Method One and Coated GDLs: (a) Cell 1 Starting From Anode Endplate, (b) Cell 3, (c) Cell 5, And (d) Cell 7

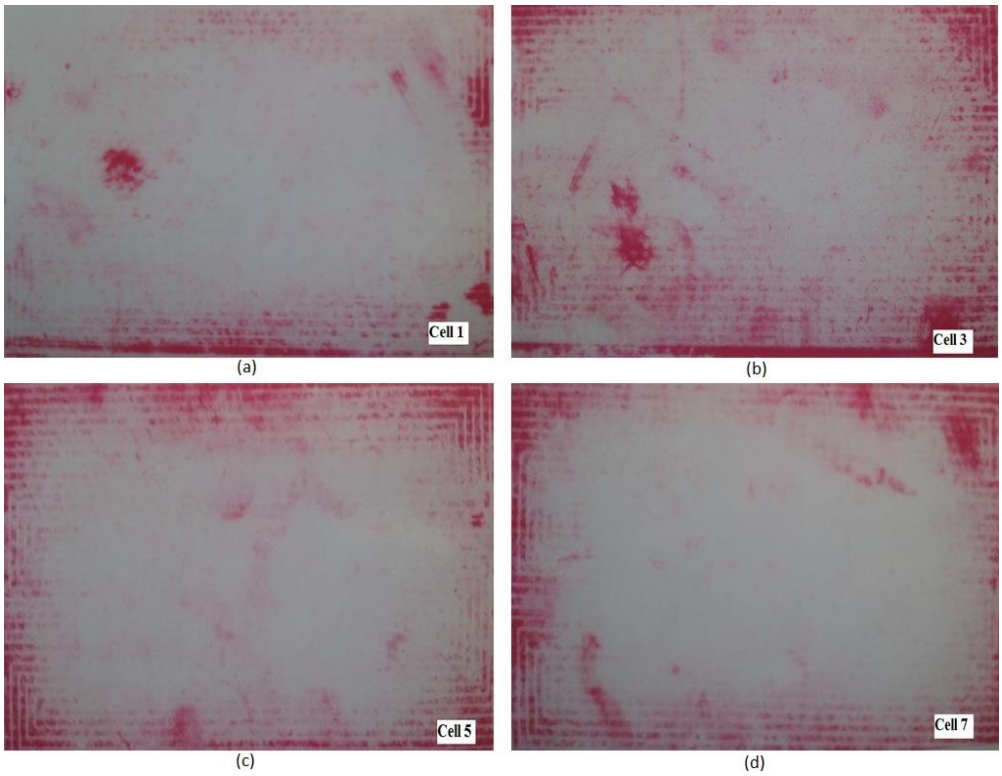

FIGURE 21 - Pressure Sensitive Film in a 16-Cell Stack Using Method Two and Coated GDLs: (a) Cell 1 Starting From Anode Endplate, (b) Cell 3, (c) Cell 5, And (d) Cell 7

Figure 22(a-d) shows the results from clamping pressure method three of cells 1, 7, 10, and 16. Cells 1 and 7, Figure 22(a) and Figure 22(b) respectively, have coated GDLs. As a result the color is deeper in the pressure-sensitive film. Figure 11 makes apparent that GDL thickness is very important in stack design because it has a large effect on compression. Method four results are shown in Figure 17(a-d) from cells 1, 7, 10, and 16. The cells containing a coated GDL, cells 1 and 7, Figure 23(a) and Figure 23(b) respectively, again have a much deeper coloration. Figure 23(a) shows better clamping pressure distribution near the endplates. Clamping pressure distribution appears to degrade toward the center of the stack while magnitude increases. Figure 23 also shows that increasing the duration of load applied at the center of the endplates significantly increases pressure applied at the GDL. This indicates that a solution to clamping pressure

concerns may be in applying a load for a set duration to the center of the endplates before operation of a FC stack. Doing this allows materials to settle and load to distribute more evenly throughout the stack. Further work must be performed to validate these claims.

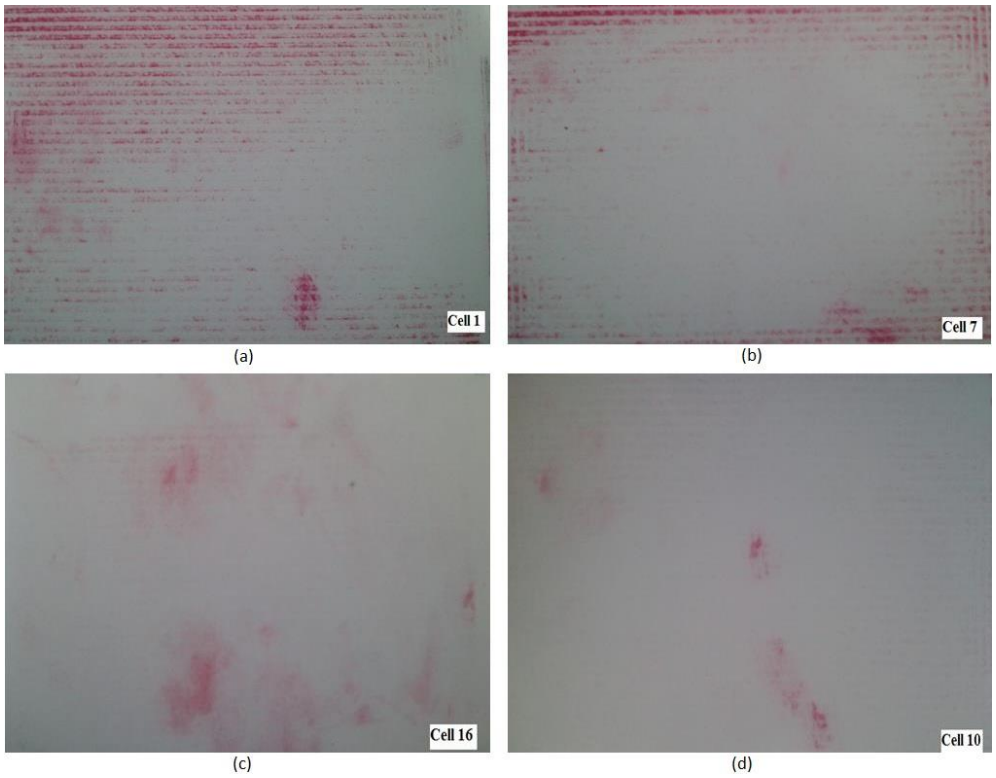

FIGURE 22 - Pressure Sensitive Film in a 16-Cell Stack Using Method Three; Coated GDLs in (a) and (b), Uncoated GDLs In (c) and (d). (a) Cell 1 Starting From Anode Endplate, (b) Cell 7, (c) Cell 16 (Cell 1 Starting From Cathode Endplate), And (d) Cell 10 (Cell 7 Starting From Cathode Endplate)

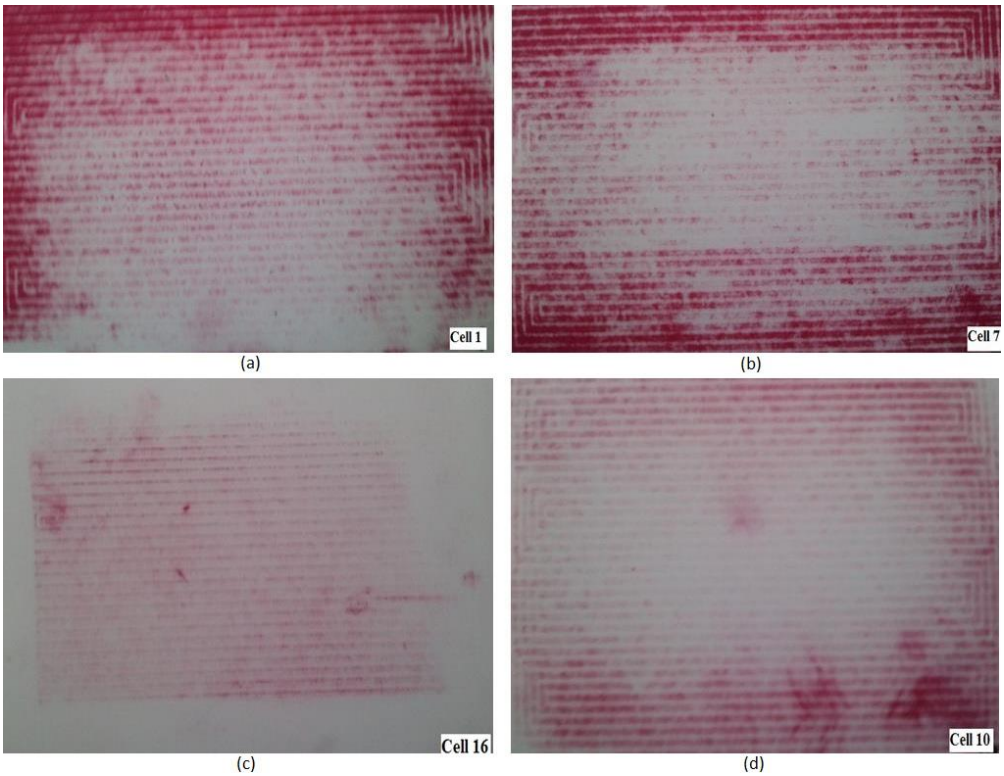

FIGURE 23 - Pressure Sensitive Film in a 16-Cell Stack Using Method Four; Coated GDLs in (a) and (b), Uncoated GDLs in (c) And (d). (a) Cell 1 Starting From Anode Endplate, (b) Cell 7, (c) Cell 16 (Cell 1 Starting From Cathode Endplate), and (d) Cell 10 (Cell 7 Starting From Cathode Endplate)

VII. CONCLUSIONS

The simulations presented provide a good foundation for the study and optimization of fuel cell systems. The novelty of the fuel cell simulation, i.e. the three-dimensional nature of the model, allows for the study of some key features not seen in other models. For instance, fluid transport in the channels and diffusion through the GDL and MEA can both be seen on the same model. Gas fraction distributions are calculated in all directions which shows the effects of channel geometry and GDL properties on mass fraction distribution; two characteristics that must be separated in 2D models. Simulation work was experimentally validated in the performance of the fuel cell by comparing the polarization curves produced. It was also shown that different fuel cell and flow pattern designs can be evaluated using the simulation developed.

Compression modeling is very important in PEM fuel cells. Adjusting bolt tension is one of the easier ways to optimize a fuel cell and so should be taken advantage of. The simulations shown here provide a 3D analysis of stress distribution in all materials of a fuel cell stack at various clamping pressure loads. Simulation of a 16-cell stack was successful and has not been previously seen in analytical work. Regions of high stress were located in the gasket between bipolar plate and MEA. The GDL stress plot reveals good contact between the channels of the bipolar plate and the carbon paper. A low region is evident in the center of each cell.

This type of simulation can be very revealing as to the effectiveness of a stack geometry and assembly. Because of the simplicity in analysis, it may be prudent for a

designer to start here in testing the validity of their design; however, full stack analysis requires significant computing power. Experimental load testing was also done on the fuel cell stack for clamping pressure at short and long time intervals and using two different compressive loads. The experimental testing performed shows a good correlation with simulation results. Overall this experimentation gives us a good idea about the distribution and magnitude of pressure across the GDLs in a 16-cell stack. The experimental testing also presented a possible solution to some clamping pressure.

VIII. RECOMMENDATIONS

Future work should focus on validating other portions of simulation work such as cell pressure and hydrogen mass fraction. Validation of hydrogen mass fraction would allow for the evaluation of hydrogen consumption at different discharge rates and for different flow plate designs. This will lead to better optimization of the fuel cell through simulation. Pressure validation would be beneficial as many modern fuel cells operate on a back pressure and purge system. Pressure allows for a higher fuel cell efficiency as more hydrogen is consumed during operation. With pressure validation, the model can be made to take into account back pressure systems.

As computing power continues to increase, it may be beneficial to begin simulations of a larger fuel cell stack considering electrochemical effects, reactant species transport, and heat transfer. When simulation work began for this thesis, simulation times were in excess of 24 hours at a cell voltage of 0.6 V. As voltage decreases, current density increases as well as the polarization of ions in the MEA. Larger concentration gradients require more elements in the thin PEM and GDL layers which significantly increases simulation time. Simulation time was reduced to 12 hours at a cell voltage of 0.4 V in recent simulations. This was a direct result of better meshing capabilities of the COMSOL program. Future simulations may be able to encompass the entire fuel cell domain.

During testing of fuel cell designs, it was found that stack compression and hydrogen sealing were very important issues. The primary reason for these issues was a

result of the fuel cell being designed for laboratory testing; which means it must be able to be disassembled and reassembled. Designs commercially available do not require this feature and can implement permanent solutions to tackle issues of compression and hydrogen sealing. Future work should focus more on working with individuals in the manufacturing field to better understand available options for compression and sealing of a fuel cell stack.

LIST OF REFERENCES

Afshari, E. and S. A. Jazayeri (2006). "Thermal Management in a PEM Fuel Cell with Phase Change Effect." WSEAS Transactions on Heat and Mass Transfer **1**(12): 808-817.

Al-Baghdadi, M. A. R. Sadiq, Al-Janabi, and H. A. K. Shahad (2007). "Modeling optimizes PEM fuel cell performance using three-dimensional multi-phase computational fluid dynamics model." Energy Conversion and Management **48**(12): 3102-3119.

Andreasen, S. J. and S. K. Kær (2009). "Dynamic Model of the High Temperature Proton Exchange Membrane Fuel Cell Stack Temperature." Journal of Fuel Cell Science and Technology **6**: 0410066-0410061 - 0041006-0410068.

Ashgari, S., H. Akhgar, and G. F. Imani (2011). "Design of thermal management subsystem for a 5kW polymer electrolyte membrane fuel cell system." Journal of Power Sources **196**: 3141-3148.

Avasarala, B. and P. Haldar (2009). "Effect of surface roughness of composite bipolar plates on the contact resistance of a proton exchange membrane fuel cell." Journal of Power Sources **188**(1): 225-229.

Bernardi, D. M. and M. W. Verbrugge (1992). "A Mathematical Model of the Solid-Polymer-Electrolyte Fuel Cell." Journal of The Electrochemical Society **139**(9): 2477-2491.

Burheim, O., P. J. S. Vie, J. G. Pharoah, and S. Kjelstrup (2010). "Ex situ measurements of through-plane thermal conductivities in a polymer electrolyte fuel cell." Journal of Power Sources **195**(1): 249-256.

Chang, W. R., J. J. Hwang, F. B. Weng, and S. H. Chan (2007). "Effect of clamping pressure on the performance of a PEM fuel cell." Journal of Power Sources **166**(1): 149-154.

Feser, J. P., A. K. Prasad, and S. G. Advani (2006). "Experimental characterization of in-plane permeability of gas diffusion layers." Journal of Power Sources **162**(2): 1226-1231.

Hashemi, F., S. Rowshanzamir, and M. Rezakazemi (2012). "CFD simulation of PEM fuel cell performance: Effect of straight and serpentine flow fields." Mathematical and Computer Modelling **55**: 1540-1557.

Heinzel, A., R. Nolte, K. Ledje-Hey, and M. Zedda (1998). "Membrane fuel cells - concepts and system design." Electrochimica Acta **43**(24): 3817-3820.

Ihonen, J., F. Jaouen, G. Lindbergh, and G. Sundholm (2001). "A novel polymer electrolyte fuel cell for laboratory investigations and in-situ contact resistance measurements." Electrochimica Acta **46**: 2899-2911.

Jiao, K. and X. Li (2010). "Cold start analysis of polymer electrolyte membrane fuel cells." International Journal of Hydrogen Energy **35**(10): 5077-5094.

Ju, H., H. Meng, and C. Y. Wang (2005). "A single-phase, non-isothermal model for PEM fuel cells." International Journal of Heat and Mass Transfer **48**(7): 1303-1315.

Karimi, G. and X. Li (2005). "Electroosmotic flow through polymer electrolyte membranes in PEM fuel cells." Journal of Power Sources **140**(1): 1-11.

Larminie, J. and A. Dicks (2006). Fuel Cell Systems Explained, Wiley.

Lee, H. S., H. J. Kim, S. G. Kim, and S. H. Ahn (2007). "Evaluation of graphite composite bipolar plate for PEM (proton exchange membrane) fuel cell: Electrical, mechanical, and molding properties." Journal of Materials Processing Technology **187–188**(0): 425-428.

Lee, K. I., S. W. Lee, M. S. Park, and C. N. Chu (2010). "The development of air-breathing proton exchange membrane fuel cell (PEMFC) with a cylindrical configuration." International Journal of Hydrogen Energy **35**(21): 11844-11854.

Lee, S.-J., C. D. Hsu, and C. H. Huang (2005). "Analyses of the fuel cell stack assembly pressure." Journal of Power Sources **145**(2): 353-361.

Li, J. Y. and S. Nemat-Nasser (2000). "Micromechanical analysis of ionic clustering in Nafion perfluorinated membrane." Mechanics of Materials **32**(5): 303-314.

Lin, J.-H., W. H. Chen, Y. J. Su, and T. H. Ko (2008). "Effect of gas diffusion layer compression on the performance in a proton exchange membrane fuel cell." Fuel **87**(12): 2420-2424.

Liu, D., L. Peng, and X. Lai (2009). "Effect of dimensional error of metallic bipolar plate on the GDL pressure distribution in the PEM fuel cell." International Journal of Hydrogen Energy **34**(2): 990-997.

Meng, H. and C.-Y. Wang (2004). "Large-scale simulation of polymer electrolyte fuel cells by parallel computing." Chemical Engineering Science **59**: 3331-3343.

Montanini, R., G. Squadrito, and G. Giacoppo (2011). "Measurement of the clamping pressure distribution in polymer electrolyte fuel cells using piezoresistive sensor arrays and digital image correlation techniques." Journal of Power Sources **196**(20): 8484-8493.

Nitta, I., T. Hottinen, O. Himanen, and M. Mikkola (2007). "Inhomogeneous compression of PEMFC gas diffusion layer: Part I. Experimental." Journal of Power Sources **171**(1): 26-36.

O'Hayre, R., S. W. Cha, W. Colella, and F. B. Prinz (2006). Fuel Cell Fundamentals. Hoboken, New Jersey, John Wiley & Sons, Inc.

Ogedengbe, E. O. B. (2009). "ThermalManagement with Solid-Fluid Slip Irreversibility Treatment in ConjugateMicrodevices." Journal of Thermodynamics **2009**.

Ramesh, P., S. S. Dimble, and S. P. Duttagupta (2011). Study of the Effect of Channel Width on Micro Fuel Cell Performance Using 3D Modeling. COMSOL Conference. Bangalore.

Sasmito, A. P., E. Birgersson, and A. S. Majumdar (2012). "A novel flow reversal concept for improved themral management in polymer electrolyte fuel cell stacks." International Journal of Thermal Sciences **54**(242-252).

Sasmito, A. P., E. Birgersson, and A.S. Majumdar (2011). "Numerical evaluation of various thermal management strategies for polymer electrolyte fuel cell stacks." International Journal of Hydrogen Energy **36**: 12991-13007.

Shahsavari, S., A. Desouza, M. Bahrami, and E. Kjeang (2012). "Thermal analysis of air-cooled PEM fuel cells." International Journal of Hydrogen Energy **37**: 18261-18271.

Sharifi Asl, S. M., S. Rowshanzamir, and M. H. Eikani (2010). "Modelling and simulation of the steady-state and dynamic behaviour of a PEM fuel cell." Energy **35**(4): 1633-1646.

Shimpalee, S. and S. Dutta (2000). "Numerical Prediction of Temperature Distribution in PEM Fuel Cells." Numerical Heat Transfer **38**: 111-128.

Strahl, S., A. Husar, and M. Serra (2011). "Development and experimental validation of a dynamic thermal and water distribution model of an open cathode proton exchange membrane fuel cell." Journal of Power Sources **196**(9): 4251-4263.

Tadbir, M. A., S. Shahsavari, M. Bahrami, and E. Kjeang (2012). THERMAL MANAGEMENT OF AN AIR-COOLED PEM FUEL CELL: CELL LEVEL SIMULATION. International Conference on Energy Sustainability & 10th Fuel Cell Science, Engineering and Technology Conference, San Diego, CA.

Tan, J., Y. J. Chao, W. K. Lee, and J. W. Van Zee (2007). "Relationship between the applied torque and compression of gasket in a fuel cell assembly." Journal of Pressure Equipment and Systems **5**(1-7).

Vural, Y., L. Ma, D. B. Ingham, and M. Pourkashanian (2010). "Comparison of the multicomponent mass transfer models for the prediction of the concentration overpotential for solid oxide fuel cell anodes." Journal of Power Sources **195**(15): 4893-4904.

Wang, H., X. Z. Yuan, and H. Li (2011). PEM Fuel Cell Diagnostic Tools, CRC Press.

Wang, X., Y. Song, and B. Zhang (2004). Pressurized Endplates for Uniform Pressure Distributions in PEM Fuel Cells. First International Conference on Fuel Cell Development and Deployment, University of Connecticut.

Wen, C.-Y., Y. S. Lin, and C. H. Lu (2009). "Experimental study of clamping effects on the performances of a single proton exchange membrane fuel cell and a 10-cell stack." Journal of Power Sources **192**(2): 475-485.

Wu, H., L. Xianguo, and P. Berg (2007). "Numerical analysis of dynamic processes in fully humidified PEM fuel cells." International Journal of Hydrogen Energy **32**(12): 2022-2031.

Yazdi, M. Z. and M. Kalbasi (2010). "A novel analytical analysis of PEM fuel cell." Energy Conversion and Management **51**(2): 241-246.

Yilanci, A., I. Dincer, and H. K. Ozturk (2008). "Performance analysis of a PEM fuel cell unit in a solar–hydrogen system." International Journal of Hydrogen Energy **33**(24): 7538-7552.

Yu, H. N., S. S. Kim, J. D. Suh, and D. G. Lee (2010). "Composite endplates with pre-curvature for PEMFC (polymer electrolyte membrane fuel cell)." Composite Structures **92**(6): 1498-1503.

Zhang, L., Y. Liu, H. Song, S. Wang, Y. Zhou, and S. J. Hu (2006). "Estimation of contact resistance in proton exchange membrane fuel cells." Journal of Power Sources **162**(2): 1165-1171.

Zhang, Y. (2007). Studies on Novel Designs of Proton Exchange Membrane (PEM). ProQuest Dissertations & Theses, University of Connecticut. **Doctor of Philosophy:** 132.

Zhang, Z., F. Désilets, V. Felice, B. Mecheri, S. Licoccia, A. C. Tavares (2011). "On the proton conductivity of Nafion–Faujasite composite membranes for low temperature direct methanol fuel cells." Journal of Power Sources **196**(22): 9176-9187.

Zhou, P., C. W. Wu, and G. J. Ma (2006). "Contact resistance prediction and structure optimization of bipolar plates." Journal of Power Sources **159**(2): 1115-1122.

Zhou, P., C. W. Wu, and G. J. Ma (2007). "Influence of clamping force on the performance of PEMFCs." Journal of Power Sources **163**(2): 874-881.

Ziogou, C., S. Voutetakis, S. Papadopoulou, and M. C. Georgiadis (2011). "Modeling, simulation and experimental validation of a PEM fuel cell system." Computers & Chemical Engineering **35**(9): 1886-1900.

Zong, Y., B. Zhou, and A. Sobiesiak (2006). "Water and thermal management in a single PEM fuel cell with non-uniform stack temperature." Journal of Power Sources **161**(1): 143-159.

VITA

Alex Martin Bates was born in Louisville, KY. After graduating from Butler Traditional High School in 2003, Alex worked full time at the manufacturing company Laminating Services Inc. In 2007 Alex began work at the United Parcel Service and entered University of Louisville to pursue a Bachelor of Science in Mechanical Engineering. In the Fall of 2011 he began research work on energy systems with Dr. Sam Park. Alex received his Bachelor of Science in Mechanical Engineering in May of 2014 and subsequently began pursuit of a Master of Engineering in Mechanical Engineering at the University of Louisville.

ALEX BATES
ambate02@louisville.edu
124 N Peterson Ave. Apt. 7
Louisville, KY 40206
Phone (Cell): 502-762-2236

OBJECTIVE
Graduate Program

EDUCATION
University of Louisville, Louisville, KY
Master of Engineering in Mechanical Engineering, Expected Degree Date: 8/2015
GPA: 3.471/4.0

University of Louisville, Louisville, KY
Bachelor of Science in Mechanical Engineering: 8/2014
GPA: 3.789/4.0

EXPERIENCE

Graduate Teaching Assistant, U of L	2014-2015
Undergraduate Research Assistant, U of L	2012-2014
Math Tutor, Math Resource Center, U of L	2011-2012
Teaching Assistant, Engineering Graphics Fundamentals, U of L	2010-2011

PRESENTATIONS
Bates Alex (2013). Open Cathode PEM Fuel Cells for Unmanned Aerial Vehicle Applications. Presented at the Fuel Cell Seminar and Energy Exposition in Columbus, OH.

PUBLICATIONS
Journal Publication
1. Santanu Mukherjee, Nicholas Schuppert, **Alex Bates**, Byungrak Son, Joogon Kim, Osung Kwon, and Sam Park, "A study of a novel Na ion battery and its anodic degradation using sodium doped Prussian blue cathode coupled with sodium deficient and rich transition metal oxide anode," Journal of Power Sources (**Submitted**).
2. **Alex Bates**, Nicholas Schuppert, Santanu Mukherjee, Byungrak Son, Joogon Kim, Dong-Ha Lee, and Sam Park, "Modeling and Simulation of 2D Lithium-Ion Solid State Battery," International Journal of Energy Research (**Submitted**)
3. Sobi Thomas, **Alex Bates**, Sang C. Lee, A.K. Sahu, and Sam Park, An Experimental and Simulation Study of Novel Channel Designs for Open-Cathode High-Temperature PEM Fuel Cells," Journal of Power Sources (**Submitted**).

4. S. Mukherjee, **A. Bates**, S.C. Lee, J. Kim, B. Son, O. Kwon, and S. Park, "A Review of Lithium and Non-lithium Based Solid State Batteries," Journal of Power Sources (**Submitted**).
5. Santanu Mukherjee, **Alex Bates**, Nicholas Schuppert, Byungrak Son, Joogon Kim, and Sam Park, "A study of the degradation characteristics of pristine and atomic layer deposited thin film metal oxide coated cathode in a solid state lithium ion battery," Journal of Solid State Electrochemistry (**In Revision**).
6. S. Mukherjee, **A. Bates**, S.C. Lee, G. Choi, and S. Park, "A Review of Application of CNTs in PEM Fuel Cells," International Journal of Green Energy (**Accepted on 11/2013**: DOI: 10.1080/15435075.2013.867270).
7. **A. Bates**, S. Mukherjee, S. Lee, and S. Park, "An Analytical Study of a Lead-Acid Flow Battery as an Energy Storage System," Journal of Power Sources: 249 (**2014**) pp. 207-218.
8. **A. Bates**, S. Mukherjee, S.W. Hwang, S.C. Lee, O. Kwon, G.H. Choi, and S. Park, "Simulation and Experimental Analysis of the Clamping Pressure Distribution in a PEM Fuel Cell Stack," International Journal of Hydrogen Energy:38 (**2013**) pp. 6481-6493.
9. **A. Bates**, S.W. Hwang, S.C. Lee, O.S. Kwon, G.H. Choi, S. Mukherjee, and S. Park, "Simulation of an Innovative Polymer Electrolyte Membrane Fuel Cell Design for Self-control Thermal Management," International Journal of Hydrogen Energy 38 (**2013**) PP. 8422-8436.
10. S. W. Hwang, G. Choi, S. Park, R. M. Ench, **A.M. Bates**, S. C. Lee, O. S. Kwon, and D. Lee, "Design Optimization of a 500W Fuel Cell Stack Weight for Small Robot Applications," Journal of the Korean Solar Energy Society, Vol. 32 No. 3. (**2012**) pp. 275-281.

Proceeding

1. **A. Bates**, S. Mukheree, S.C. Lee, O.S. Kwon, S. Ha, S. Thomas, D. Lee, and Sam Park, "A High Energy Density System by Thin Metallic Bipolar Plates," ECS Transactions (2013) 58(1): 223-227; doi:10.1149/05801.0223ecst.
2. S. Mukheree, **A. Bates**, S.C. Lee, O.S. Kwon, S. Ha, and Sam Park, "Analysis of Electrochemical Properties of ZnBr Flow Battery," ECS Transactions (2013).
3. **A. Bates**, S. Mukheree, S.C. Lee, O.S. Kwon, S. Ha, S. Thomas, D. Lee and Sam Park, "Open Cathode PEM Fuel Cells For Unmanned Arial Vehicle (UVA) applications," Fuel Cell Seminar 2013.
4. **A. Bates**, S. Ha, S.C. Lee, O. Kwon, S. Park, and D. Lee "Design and Simulation of Low Weight Fuel Cell Stack for a Mobile Robot Application," Proceedings of the KSES 2013 Spring Annual Conference, pp.82-87.
5. O.S. Kwon, S.C. Lee, D.H. Lee, B. Han, S.W. Hwang, G.H. Choi, S. Mukherjee, **A. Bates**, and S. Park, "Development of a High Performance MEA using Current-

sensing Atomic Force Microscopy (CS-AFM) and Nano-scale Impedance Spectroscopy (NIS)," ECS Transactions Vol. 50 (2012).

6. S.W. Hwang, G.H. Choi, **A. Bates**, R.M. Ench, S.C. Lee, O.S. Kwon, D.H. Lee, S. Mukherjee, and S. Park, "A Novel Lightweight Polymer Electrolyte Fuel Cell Stack for Robot Systems," ECS Transactions Vol. 50 (2012).
7. S.W. Hwang, G.H. Choi, S.C. Lee, O.S. Kwon, D.H. Lee, **A. Bates**, R.M. Ench, and S. Park, "Design and Development of a Fuel Cell Stack for Hybrid Power Systems in Small Robot Application." The 9th International Conference on Ubiquitous Robots and Ambient Intelligence (URAI 2012) in Daejeon, Korea from November 26 to 29, 2012.
8. S. W. Hwang, G. H. Choi, S. Park, R. M. Ench, **A.M. Bates**, S. C. Lee, O. S. Kwon, and D. H. Lee, "Optimization of a Fuel Cell Stack for Small Robot Systems," at the 3rd International Fuel Cell Forum, March 29th 2012, Daegu, Republic of Korea.

SKILLS AND QUALIFICATIONS

- Comsol
- SolidWorks
- Matlab
- Ansys
- SEM and XRD